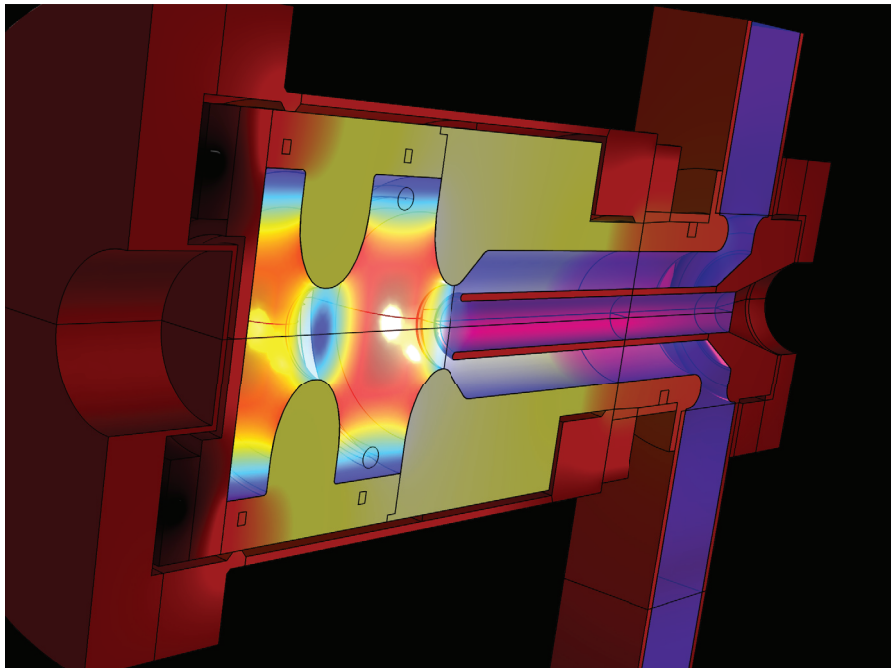


# MODELLING RF-PHOTOGUNS

*A Numerical and Experimental study  
of Thermal and Electromagnetic behaviour*



ING. D.J. (DURK) DE VRIES

*Master of Science (MSc)*

Groningen – Eindhoven, November 2011 – September 2012

ing. D.J. (Durk) de Vries: *Modelling RF-Photoguns*, A Numerical and Experimental study of Thermal and Electromagnetic behaviour.

**SUPERVISORS:**

dr. ir. J.P.M. (Hans) Beijers

dr. ir. G.J.H. (Seth) Brussaard

**INSTITUTE, FACULTY, UNIVERSITY:**

Nuclear-physics Accelerator Institute (KVI)

Faculty of Mathematics and Natural Sciences (FWN)

University of Groningen (RUG)

**COLLABORATING UNIVERSITIES:**

University of Groningen (RUG)

Eindhoven University of Technology (TU/e)

**LOCATION, TIME FRAME:**

Groningen – Eindhoven

November 2011 – September 2012

## CONTENTS

---

<b>1</b>	<b>INTRODUCTION</b>	<b>1</b>
1.1	X-ray free electron lasers	1
1.2	Normal conductance and high rep-rates	1
1.3	Scope of this project	2
<b>2</b>	<b>THEORETICAL ASPECTS</b>	<b>3</b>
2.1	Inner workings	3
2.2	Lumped element description	4
2.2.1	Model building	5
2.2.2	Model fitting	6
2.3	Multiphysics	7
2.3.1	Field equations and boundary conditions	9
2.3.2	Important considerations	11
<b>3</b>	<b>NUMERICAL STUDY</b>	<b>13</b>
3.1	Numerical methods	13
3.2	Optimisations	13
3.3	Basic validation	15
3.3.1	Eigenfrequency	15
3.3.2	Wall conductance	18
3.4	Tuning	19
3.4.1	PPF-Scans	20
3.4.2	Results	25
3.4.3	Discussion	25
3.5	Examples	26
<b>4</b>	<b>EXPERIMENTAL STUDY</b>	<b>27</b>
4.1	Setup	27
4.1.1	Network analyser	28
4.1.2	Temperature control	28
4.1.3	Multichannel thermometer	29
4.2	Temperature gradient measurements	30
4.2.1	Measuring	31
4.2.2	Modelling	31
4.2.3	Discussion	32
4.3	Reflection measurements	34
4.3.1	Measuring	34
4.3.2	Modelling	35
4.3.3	Discussion	38
4.4	Phase thermostration	39
4.4.1	Measuring	39
4.4.2	Discussion	39

<b>5</b>	<b>CONCLUSIONS AND RECOMMENDATIONS</b>	<b>43</b>
<b>A</b>	<b>NUMERICAL METHODS</b>	<b>45</b>
A.1	Heat equation	45
A.2	Standard form	46
A.3	Finite difference method	47
A.4	Finite element method	48
<b>B</b>	<b>EXAMPLES</b>	<b>51</b>
B.1	3D RF-PScan (coupler, rectport)	51
B.2	2D RF-Sim (cavity, coaxport)	52
B.3	3D RF-Sim (cav+coup, rectport)	53
B.4	2D Heat-Sim (cavity, coaxport)	54
B.5	3D Heat-Sim (cav+coup, rectport)	55
<b>C</b>	<b>MULTICHANNEL THERMOMETER</b>	<b>57</b>
C.1	Device	57
C.2	Operation	58
C.3	Calibration	59
C.4	Discussion	60
	<b>BIBLIOGRAPHY</b>	<b>63</b>



## LIST OF FIGURES

---

Figure 1.1	Schematic representation of an RF-photogun.	1
Figure 2.1	The 0-mode and $\pi$ -mode of a 1.5-cell cavity.	4
Figure 2.2	Lumped element description of a cavity.	5
Figure 2.3	Fitted magnitude and phase curves.	6
Figure 2.4	Relation H-field, geometry and Q-dissipation.	7
Figure 2.5	The three stages of the coupled simulation.	8
Figure 2.6	Locations of the domains and boundaries.	9
Figure 3.1	The cavity as a 2D or 3D problem.	14
Figure 3.2	The spatial distribution of mesh points.	15
Figure 3.3	Convergence of the eigenfrequency.	16
Figure 3.4	The magnetic current and the lossy dielectric.	17
Figure 3.5	Influence of conductance on E-freq. & E-field.	18
Figure 3.6	Magnetic field, heat production along the wall.	19
Figure 3.7	Use of polynomial interpolation to find $f_e$ .	22
Figure 3.8	Minimum in $P(x)$ , dataset border definition.	23
Figure 4.1	Photo of the TU/e 1.5-cell S-band gun.	27
Figure 4.2	Location of the gun's heat sources and sinks.	28
Figure 4.3	Normal and thermal image of the heating wire.	29
Figure 4.4	Location of the used temperature sensors.	30
Figure 4.5	Two LM35 sensors clamped against a flange.	30
Figure 4.6	Temperatures applied as boundary conditions.	32
Figure 4.7	Measured, simulated temperatures compared.	33
Figure 4.8	Comparison measurement and simulation A.	35
Figure 4.9	The parameters of the absorption spectrum.	36
Figure 4.10	Comparison measurement and simulation B.	37
Figure 4.11	Temp. dependence $\Delta R_L$ , location of steel rim.	38
Figure 4.12	Temperature reading with phase values.	40
Figure 4.13	Phase curve near point of optimum coupling.	41
Figure B.1	Electric field plot of the input coupler (3D).	51
Figure B.2	Electric field plot of the cavity (2D).	52
Figure B.3	Electric field plot of cavity and coupler (3D).	53
Figure B.4	Thermal plot of the cavity (2D).	54
Figure B.5	Thermal plot of the cavity (3D).	55
Figure C.1	The LM35 sensor attached to shielded cable.	57
Figure C.2	Thermometer with calibration rings.	58
Figure C.3	GUI of the demultiplexing software.	58
Figure C.4	Calibration setup with insulation removed.	59
Figure C.5	Test reading without thermostrotration.	61

## LIST OF TABLES

---

Table 3.1	PPF-scan results compared to TU/e values.	24
Table 4.1	Temperatures during reflection experiments.	34
Table 4.2	Spectrum values and correction factors.	37
Table 4.3	Results obtained using a reduced steel rim.	39
Table C.1	Values a and b determined for channels 1-7.	60
Table C.2	Values a and b determined for channels 8-14.	60

## ACRONYMS

---

FDM	Finite Difference Method
FEM	Finite Element Method
FWN	Faculteit Wiskunde en Natuurwetenschappen
GUI	Graphical User Interface
KVI	Kernfysisch Versneller Instituut
PI	Proportional-Integral
PPF	Parameter-Power-Frequency
RF	Radio Frequency
RLC	Resistor-Inductor-Capacitor
RUG	Rijks Universiteit Groningen
TU/e	Technische Universiteit Eindhoven
XFEL	X-ray Free Electron Laser
ZFEL	Zernike Free Electron Laser



## INTRODUCTION

### 1.1 X-RAY FREE ELECTRON LASERS

In recent years, a large interest in high rep-rate X-ray Free Electron Lasers (XFELs) has stimulated the development of high rep-rate high quality electron sources (here, rep-rate refers to repetition rate; the number of electron pulses per second):

Inside a free electron laser, relativistic electron bunches are guided through an undulator that forces the electrons to emit synchrotron radiation. Given that the electron beam's emittance is sufficiently small ( $\leq 1\text{mm} \cdot \text{mrad}$ , where emittance refers to the spread in phase space of the electrons), the radiation is emitted in the form of a parallel coherent laser beam. Since the electron beam's emittance cannot be improved along the beam line, requiring a beam of low emittance implies requiring an electron source of high quality.

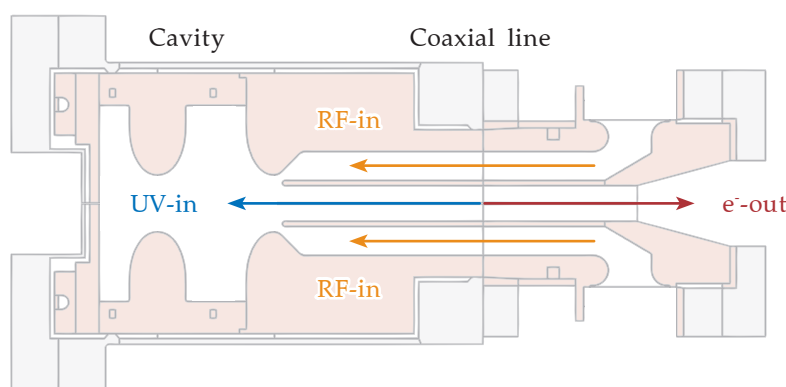


Figure 1.1: Schematic representation of an RF-photogun.

There are only two types of sources known to be capable of delivering the required quality, one of them being the RF-photogun. Here, particular interest goes to normal conducting guns (since they can sustain stronger acceleration fields than super conducting ones) that support high rep-rates (some applications require the laser to support high rep-rates).

### 1.2 NORMAL CONDUCTANCE AND HIGH REP-RATES

Normal conducting high rep-rate RF-photoguns still only exist on the drawing table. Their design includes an excitation laser that expels electrons from a cathode (just like low rep-rate photoguns, [Figure 1.1](#)). These electrons are then accelerated from approximately zero up to

extreme-relativistic speeds (4-7MeV [3, p. 42]), by a standing electromagnetic wave pattern inside a 1.5 or 2.5-cell copper cavity. To produce electron bunches of the required quality, field strengths of 100-120MV/m are applied. Unlike low rep-rate guns however, they should repeat their shots with rates up to 1kHz (currently, photoguns are typically limited to about 360Hz or less). Since their cavity walls are normal conducting, large amounts of internal heat will be generated during their operation: 16-18kW [1] is dissipated into a volume the size of a cookie jar.

When combining this with the fact that RF-photoguns are notoriously sensitive to temperature (the resonance frequency shifts with a rate of 50kHz/°C [3, p. 65]), we can see that the development of such a photogun will be an interesting engineering challenge: Even though heat fluxes of up to 225MW/m<sup>2</sup> [1] will flow through the cavity walls (with the potential of causing significant temperature differences), the temperature should remain uniform and constant up to 0.05°C [4, p. 56]. The best (and perhaps the only) way to achieve this, is by designing the cavity's cooling channels in such a way that the spatial distribution of the cooling capacity matches the spatial distribution of the current density in the cavity walls.

### 1.3 SCOPE OF THIS PROJECT

As part of a design study for a compact high rep-rate soft X-ray Free Electron Laser at the University of Groningen (ZFEL), we have performed a numerical and experimental study of the thermal and electromagnetic behaviour of RF-photoguns. More specifically, we have developed numerical models (finite element) that support the basic (multi) physics, reproduce existing (low rep-rate) results and allow for studies in the high rep-rate domain.

Apart from using different solving methods, cavity theory and common sense to validate our results, we have tried to benchmark our numerical models experimentally: We have done extensive measurements of thermal and electromagnetic behaviour of an existing normal conducting low rep-rate gun from the Eindhoven University of Technology (TU/e). We have performed the first half of our research in Groningen at the KVI (developing models), the other half has been done in Eindhoven at the TU/e (comparing simulations to actual measurements).

This thesis presents both the numerical and experimental work: In order to introduce and grasp the subject, it starts with a theoretical approach (Chapter 2). Then, it proceeds by treating several aspects of modelling (Chapter 3, roughly representing the work done in Groningen) and measuring (Chapter 4, representing the work done in Eindhoven). Finally, in Chapter 5 we present some conclusions and recommendations for future work.

## THEORETICAL ASPECTS

---

This chapter starts by treating the inner workings of an RF-photogun, using our TU/e gun as an example; [Section 2.1](#). We then proceed with an analytical description using a lumped element model ([Section 2.2](#)), and finish with a treatment of the multiphysics approach ([Section 2.3](#)).

### 2.1 INNER WORKINGS

The gun we have investigated at the TU/e in Eindhoven is a normal conducting low rep-rate 1.5-cell 2.998GHz S-band gun. During operation, its cavity is thermostated at  $40.00 \pm 0.05^\circ\text{C}$ . About three times a second, a pulse of electromagnetic energy from a klystron flows from the right through the coaxial line and reaches the cavity's first iris ([Figure 1.1](#)). These pulses should have a peak height of about 8.5MW and a full-width half-maximum of  $3\mu\text{s}$  (in reality however, they're usually limited to about 4.1MW, mainly because of discharges occurring inside the cavity and waveguides [[4](#), p. 62]).

Assuming that the system is at perfect resonance (and that the impedances between cavity and transmission line match), all incident power will be dissipated into the cavity's walls (no reflections will occur). The average power dissipated is determined by the amount of energy contained in a single pulse (about 25J) times the number of pulses per second (3Hz). This means that about 75W of power is dissipated on average, causing little or no change in the cavity's geometry (no temperature gradients, no deformation; typical behaviour for low rep-rate guns).

This power dissipation is primarily caused by a standing wave pattern that forms inside the cavity, having two fundamental modes (in a 1.5-cell cavity, the single pillbox's  $\text{TM}_{010}$ -mode splits up in two): The 0-mode, in which the fields inside both cells oscillate in phase (at about 2.992GHz, [Figure 2.1](#) on the left) and the  $\pi$ -mode, in which they oscillate in antiphase (at about 2.998GHz). Of these two modes, the  $\pi$ -mode is the one suitable for particle acceleration. Here, the on-axis electrical field vectors in the right cell will be of equal and opposite size relative to the ones in the left cell.

Indeed. Suppose at some point in time the electric field strength has reached its peak while a bunch of electrons is expelled from the cathode by an excitation laser: The bunch will start accelerating towards the left iris, while the electric field reduces in strength (since it oscillates). Then, one quarter of an oscillation period later, the mo-

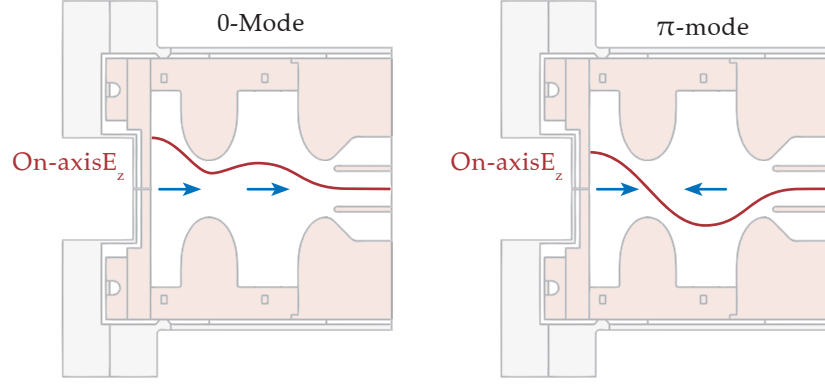


Figure 2.1: The 0-mode and  $\pi$ -mode of a 1.5-cell cavity.

ment the bunch crosses the left iris, the field changes sign. By the time the bunch enters the second cell, the field configuration will have changed in such a way that the electrons will be accelerated once more.

Bunch charges are typically on the order of 1nC or less, and the final kinetic energy of the electrons is about 3.0MeV. This corresponds to maximum field strengths of about 76MV/m (the design values are 4.4MeV and 110MV/m respectively).

## 2.2 LUMPED ELEMENT DESCRIPTION

The simplest way to model our cavity's resonance behaviour is by using a lumped element description (Figure 2.2). Here, the coaxial line is modelled by a source impedance  $Z_{src}$  and the cells are modelled by parallel RLC circuits (harmonic oscillators). The resistors in these circuits represent the dissipation into the walls, the inductors represent the magnetic fields and the capacitors represent the electric fields. To model the coupling irises, inductors ( $Z_\alpha$ ,  $Z_\beta$ ) are used.

If we now substitute the impedance of the total load given by

$$Z_l(\omega) = \left( \frac{1}{Z_1 + Z_\alpha} + \frac{1}{Z_2} \right)^{-1} + Z_\beta$$

(where  $\frac{1}{Z_1} = \frac{1}{R_1} + \frac{1}{i\omega L_1} + i\omega C_1$  and  $\frac{1}{Z_2} = \frac{1}{R_2} + \frac{1}{i\omega L_2} + i\omega C_2$ ) into the equation for the complex reflection coefficient defined as

$$\Gamma(\omega) \equiv \frac{Z_l(\omega) - Z_{src}}{Z_l(\omega) + Z_{src}},$$

we can plot the relative magnitude and phase of the reflected power as a function of frequency:

$$P(f) \equiv \Gamma_{dB}(2\pi f) = 10 \log_{10} |\Gamma(\omega)|^2, \quad (2.1)$$

$$\varphi(f) \equiv \Gamma_o(2\pi f) = \frac{360}{2\pi} \arg(\Gamma(\omega)). \quad (2.2)$$

The resulting curves will prove to be a very effective tool when trying to determine the behaviour of a resonant structure.



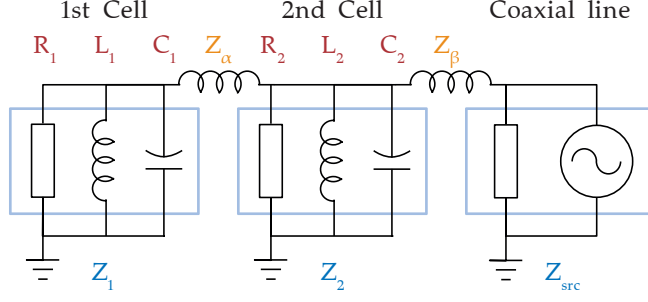


Figure 2.2: Lumped element description of a 1.5-cell cavity.

### 2.2.1 Model building

To illustrate the power of this simple model, we will pick one of the measurements from our 1.5-cell TU/e gun, and see if we can achieve the same results by strategically choosing the values of the different lumped elements. In order to do this we will need some rules of thumb, mostly coming from classical cavity theory [2, p. 334]. We will not treat classical cavity theory here, as many others have already done so. Instead, we will just list the relevant concepts and equations and use them to build our model.

We start by estimating the angular eigenfrequencies of both cells: Since each cell loosely resembles a pillbox cavity, we use the pillbox cavity resonance frequency relation;

$$\tilde{\omega}_1^0 = \frac{\tilde{p}_{01}}{r_1 \sqrt{\mu\epsilon}} \approx 2\pi \cdot 2.749 \cdot 10^9 \text{ Rad/s}, \quad (2.3)$$

$$\tilde{\omega}_2^0 = \frac{\tilde{p}_{01}}{r_2 \sqrt{\mu\epsilon}} \approx 2\pi \cdot 2.751 \cdot 10^9 \text{ Rad/s}, \quad (2.4)$$

where  $\tilde{p}_{01}$  represents the first root of the zeroth order Bessel function (2.405) and  $r_1, r_2$  are the radii of the left and right cell respectively (note that  $\tilde{\omega}_1^0, \tilde{\omega}_2^0$  approximate the eigenfrequencies of the two separate RLC circuits, not the eigenfrequencies of the circuit as a whole).

We then proceed by determining the unloaded quality factor [3, p. 38], [2, p. 356] and shunt-impedance [3, p. 29]. The quality factor of normal conducting cavities is usually between  $1 \cdot 10^4$  and  $2 \cdot 10^4$ . Although any value in this interval would suffice to prove our point, the ones coming from our simulations (Table 3.1) should yield the best results. Since the same goes for the shunt-impedance, we set  $Q_{ul} \approx 11.580 \cdot 10^3$  and  $R_{sh} \approx 50.327 \cdot 10^6 \Omega/\text{m}$  for both cells.

Using the shunt-impedance, we can now determine the values of  $R_1$  and  $R_2$ . If we rewrite the shunt-impedance's definition;  $R_{sh} \equiv U_0^2/P_{loss}l_c$ , we can determine the total power loss;  $P_{loss} = U_0^2/R_{sh}l_c$ . We also know that most of this power will be dissipated in the cylindrical outer surfaces of the cells. Since the right cell is twice as long as the left one, two third is dissipated in the right and one third is dissipated in the left cell.

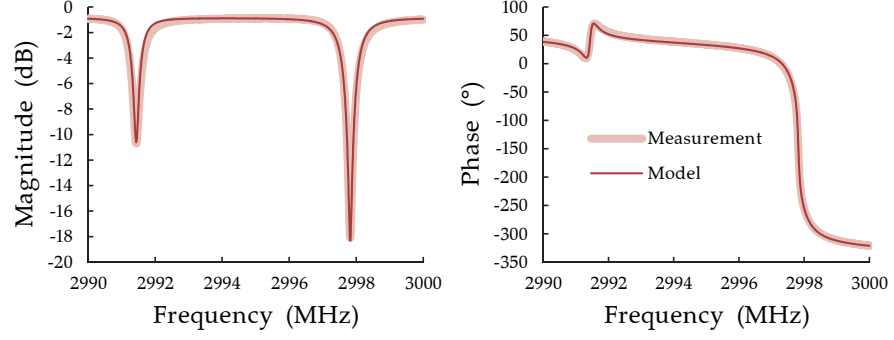


Figure 2.3: Fitted magnitude and phase curves.

Combining these results with the standard power loss equation for resistors;  $P_{\text{loss}} = U\bar{U}/2R = U_0^2/2R$ , gives the values  $R_1$  and  $R_2$ :

$$\frac{1}{3}P_{\text{loss}} = \frac{U_0^2}{3R_{\text{sh}}l_c} = \frac{U_0^2}{2R_1} \therefore R_1 = \frac{3}{2}R_{\text{sh}}l_c \approx 5.662 \cdot 10^6 \Omega,$$

$$\frac{2}{3}P_{\text{loss}} = \frac{2U_0^2}{3R_{\text{sh}}l_c} = \frac{U_0^2}{2R_2} \therefore R_2 = \frac{3}{4}R_{\text{sh}}l_c \approx 2.831 \cdot 10^6 \Omega.$$

The values for  $L_1$ ,  $L_2$ ,  $C_1$  and  $C_2$  can be estimated by using the equations for eigenfrequencies and quality factors. Since both cells are modelled with parallel RLC circuits, we use  $\omega^0 = 1/\sqrt{LC}$  and  $Q = R\sqrt{C/L}$  and find

$$\tilde{L}_1 = \frac{R_1}{Q_{\text{ul}}\tilde{\omega}_1^0} \approx 2.831 \cdot 10^{-8} \text{H}, \quad \tilde{L}_2 = \frac{R_2}{Q_{\text{ul}}\tilde{\omega}_2^0} \approx 1.414 \cdot 10^{-8} \text{H},$$

$$\tilde{C}_1 = \frac{Q_{\text{ul}}}{R_1\tilde{\omega}_1^0} \approx 1.184 \cdot 10^{-13} \text{F}, \quad \tilde{C}_2 = \frac{Q_{\text{ul}}}{R_2\tilde{\omega}_2^0} \approx 2.366 \cdot 10^{-13} \text{F}.$$

To complete our model, we set the source impedance  $Z_{\text{src}}$  equal to the characteristic impedance of the coaxial feeding line ( $Z_{\text{src}} = 50\Omega$ ). The values  $Z_\alpha$  and  $Z_\beta$  are determined by fitting.

### 2.2.2 Model fitting

By putting our model in suitable plotting software, we have fitted the magnitude and phase curves (Equation 2.1 and Equation 2.2) to one of our measurements (Section 4.3.1) using four fitting parameters;  $L_\alpha$ ,  $L_\beta$ ,  $\omega_\alpha$  and  $\omega_\beta$  (Figure 2.3):

$$Z_\alpha = i\omega L_\alpha, \quad Z_\beta = i\omega L_\beta,$$

$$\omega_1^0 = \tilde{\omega}_1^0 + \omega_\alpha - \frac{1}{2}\omega_\beta, \quad \omega_2^0 = \tilde{\omega}_2^0 + \omega_\alpha + \frac{1}{2}\omega_\beta,$$

$$L_1 = \frac{R_1}{Q_{\text{ul}}\omega_1^0}, \quad L_2 = \frac{R_2}{Q_{\text{ul}}\omega_2^0}, \quad C_1 = \frac{Q_{\text{ul}}}{R_1\omega_1^0}, \quad C_2 = \frac{Q_{\text{ul}}}{R_2\omega_2^0},$$

with  $L_\alpha$  and  $L_\beta$  the inductances used to model the coupling irises and  $\omega_\alpha$ ,  $\omega_\beta$  the correction factors for the eigenfrequencies given by Equation 2.3 and Equation 2.4.

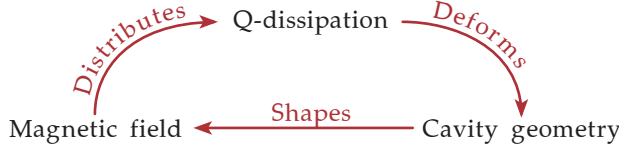


Figure 2.4: Relation between H-field, geometry and Q-dissipation.

Using strategically chosen (first) estimates and root finding algorithms, we have found the following values for the fit parameters:

$$\begin{aligned} L_\alpha &\approx 9.508 \cdot 10^{-6} \text{H}, & L_\beta &\approx 4.678 \cdot 10^{-7} \text{H}, \\ \omega_1^0 &\approx 1.087387 \cdot \tilde{\omega}_1^0, & \omega_2^0 &\approx 1.073186 \cdot \tilde{\omega}_2^0. \end{aligned}$$

These values suggest that our initial estimates for  $\omega_1^0$  and  $\omega_2^0$  were off by about 8% (admittedly, these results could just as well have been attributed to errors in  $Q_{ul}$  or  $R_{sh}$ ).

The point we want to make here is that the resonance behaviour of a cavity can be described using a fairly simple analytical model (even when using rather crude initial estimates for its input values). In terms of cavity geometry optimisation however, analytical models have almost no predictive value when compared to the numerical models that will be introduced in the next subsection.

### 2.3 MULTIPHYSICS

A more comprehensive way of modelling the behaviour of the cavity is by numerically solving the coupled partial differential equations describing electromagnetic wave propagation, heat production and transport and thermal expansion. These processes are coupled as illustrated schematically in [Figure 2.4](#):

1. The electromagnetic field distribution is determined by the cavity's geometry. This determines the distribution of electromagnetic power deposited into the cavity's walls.
2. The cavity's geometry is deformed by thermal expansion.
3. The deformations change the electromagnetic field distribution and thus the distribution of power deposited into the walls.

When the power distribution generated in the deformed cavity equals the power distribution causing the cavity deformation, the system reaches a stationary state. It is this stationary state we will try to simulate; we will not consider any transient effects. Since we have to calculate electromagnetic wave propagation, heat conduction and thermal expansion simultaneously in the same 3D structure, the problem may become quite intricate and maybe too large considering our limited computational resources ([Section 3.2](#)).

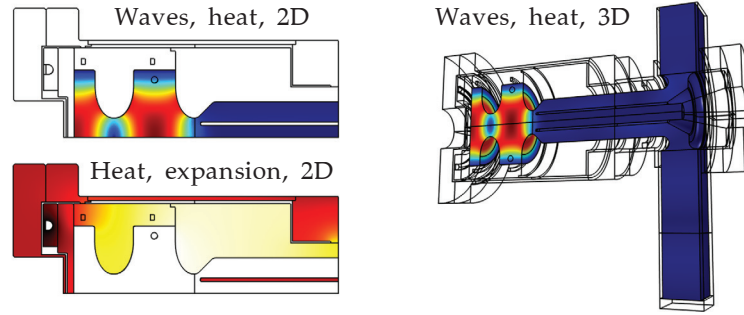


Figure 2.5: The three stages of the coupled simulation.

However, it is possible to partly decouple the system: Since the occurring deformation is on the order of several micrometres (i.e. small with respect to our typical length scale, even for high rep-rate situations), the deformation of the electromagnetic field and the deformation of the walls surrounding it will be practically the same (given that the system is kept at resonance). In other words, the two (field and wall) will deform together in the same way. We may therefore assume that, regarding the interaction between field and wall, the effects of thermal expansion can be neglected. The resulting simulation is done in three stages (Figure 2.5):

1. First, we perform a coupled electromagnetic wave and heat conduction simulation, where electromagnetic power is injected at resonance (using the coaxial line). The wave equation is solved to determine the field distribution and the resulting dissipation of electromagnetic energy into the cavity walls. The distribution of the dissipated energy is used to determine the heat transport and the resulting temperature distribution (note that deformation is not included here).
2. The computed temperature distribution is then used to determine the cavity deformation caused by thermal expansion (here, we will not include electromagnetic waves). During this second stage the temperature is regarded as a local material property. The temperature distribution and the cavity's geometry will therefore deform in the same way.
3. The deformed cavity geometry is used in a third stage to perform again a coupled electromagnetic wave and heat conduction simulation (at the new resonance frequency). The resulting heat distribution is used to test the system for self-consistency: It should be equal to the deformed version obtained in the second stage. In this case the system is in a stationary state.

Simulations like the one described above are referred to as multi-physics simulations. Although most modern simulation packages in-

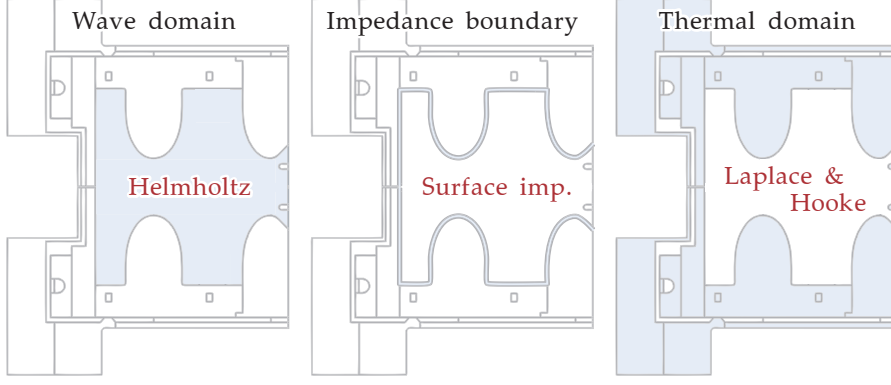


Figure 2.6: Locations of the respective domains and boundaries.

corporate some form of multiphysics, we have chosen Comsol Multiphysics<sup>1</sup>, since it appears to be the most flexible one. Comsol uses the finite element method as its mathematical cornerstone (Appendix A). The various fields (electromagnetic, temperature and material displacement) are calculated by solving the corresponding partial differential equations subject to appropriate boundary conditions.

### 2.3.1 Field equations and boundary conditions

Before presenting and discussing the results of these multiphysics simulations, we will first introduce and examine some of the used field equations and boundary conditions. We treat the different processes by following the flow of energy: We start with electromagnetic waves and then proceed with dissipation, heat flow, temperature distribution and expansion.

In Comsol, the electric field distribution  $\vec{E}(\vec{r})$  in the photogun is determined using a generalized Helmholtz equation and appropriate boundary conditions (Figure 2.6);

$$\nabla \times \mu_r^{-1} (\nabla \times \vec{E}) - k_0^2 \left( \epsilon_r - \frac{i\sigma}{\omega\epsilon_0} \right) \vec{E} = 0, \quad (2.5)$$

assuming a harmonic time variation. Here,  $\epsilon_r$  and  $\mu_r$  are the relative permittivity and permeability of the medium through which the wave propagates and  $\sigma$  is its electrical conductivity. The value  $k_0 = \omega\sqrt{\epsilon_0\mu_0}$  refers to the vacuum wave number with  $\epsilon_0$  and  $\mu_0$  the permittivity and permeability of the vacuum. Equation 2.5 follows directly from Faraday's law,  $\nabla \times \vec{E} = -\partial\vec{B}/\partial t$ , and Ampère-Maxwell's law,  $\nabla \times \vec{B} = \mu\vec{j} + \epsilon\mu\partial\vec{E}/\partial t$ , with  $\vec{j} = \sigma\vec{E}$ . It is solved in the vacuum region of the photogun where  $\mu_r = 1$ ,  $\epsilon_r = 1$  and  $\sigma = 0\text{S/m}$ .

Inside the walls (near the surface) the oscillating magnetic field decays exponentially (due to the finite conductivity  $\sigma = 5.91 \cdot 10^7\text{S/m}$  of the copper cavity walls [2, p. 336]) with a spatial scale length given by

<sup>1</sup> <http://www.comsol.com/>

the skin depth  $\delta = \sqrt{2/\mu\omega\sigma}$  (the skin depth of copper at a frequency of  $\omega = 2\pi 3\text{GHz}$  is  $1.2\mu\text{m}$ ). The magnetic field induces a current density  $\vec{J}_s$  that decays exponentially as well (that is,  $\vec{J}_s \propto e^{-\xi/\delta}$ , with  $\xi$  a perpendicular depth coordinate). Since  $\delta$  is small with respect to the cavity's dimensions, we may define an effective surface current

$$\vec{K}_{\text{eff}} = \int_0^\infty \vec{J}_s d\xi = \vec{n} \times \vec{H}_\parallel, \quad (2.6)$$

assumed to exist only at the boundary (we may omit  $\vec{H}_\perp$  here; since we have  $\sigma \gg \varepsilon = \varepsilon_0$ , our approximation may neglect electrostatics [2, p. 337]). The resulting boundary condition

$$Z_s \vec{n} \times \vec{H}_\parallel + \vec{E}_\parallel = 0, \quad (2.7)$$

is known as the impedance boundary condition (Figure 2.6), with  $\vec{n}$  a unit vector normal to the boundary surface and  $\vec{H}_\parallel$ ,  $\vec{E}_\parallel$  the tangential magnetic and electric field components at the boundary ( $\vec{E}_\perp$  is omitted, since  $\sigma \gg \varepsilon = \varepsilon_0$ ). The value  $Z_s = \sqrt{i\omega\mu/\sigma} = (1+i) \sqrt{\omega\mu/2\sigma} = \omega\mu\delta(1+i)/2 = (1+i)/\sigma\delta$ , the coefficient of proportionality linking  $\vec{E}_\parallel$  and  $\vec{K}_{\text{eff}}$  is known as the surface impedance [2, p. 339] (actually, Comsol's implementation uses a more general version of the impedance boundary condition that includes electrostatics as well).

Since  $\lim_{\sigma \rightarrow \infty} Z_s(\sigma) = 0$ , perfectly conducting walls will have  $\vec{E}_\parallel = 0$ . This means that the electrical field along the surface induced by the electromagnetic waves will be completely cancelled by an induced field of equal and opposite size. In case of normally conducting walls however,  $\vec{E}_\parallel$  will be finite and a current  $\vec{K}_{\text{eff}}$  will dissipate power at the boundary equal to

$$\frac{\partial P_{\text{loss}}}{\partial a} = \frac{1}{2\sigma\delta} |\vec{K}_{\text{eff}}|^2, \quad (2.8)$$

with  $\partial P_{\text{loss}}/\partial a$  denoting the electromagnetic power loss per unit surface area at the boundary.

Since this power is dissipated in the form of heat, it is described as a heat flux  $\vec{q} = -k\nabla T$  in  $\text{W}/\text{m}^2$  at the boundary (with  $k$  the thermal conductivity): It is inserted directly into the thermal simulation as a Neumann boundary condition. Together with several Dirichlet boundary conditions (boundaries with known temperature), some insulating boundary conditions and the Laplace equation ( $\nabla^2 T = 0$ ), it will completely determine the stationary temperature distribution.

Using the calculated temperature field  $T(\vec{r})$ , the cavity deformation caused by thermal expansion and elastic strains can be determined: The thermal strain tensor is given by  $\hat{\varepsilon}_{\text{th}} = \alpha(T - T_{\text{ref}})\hat{I}$ , with  $\alpha$  the thermal expansion coefficient,  $T_{\text{ref}}$  the temperature at which there are no thermal stresses and  $\hat{I}$  the 3D unit tensor. The total strain tensor is defined as the sum of the elastic and thermal strain tensors, i.e.

$$\hat{\varepsilon} \equiv \frac{1}{2} (\nabla \vec{u} + \nabla \vec{u}^T) = \hat{\varepsilon}_{\text{el}} + \hat{\varepsilon}_{\text{th}}, \quad (2.9)$$

with  $\nabla \vec{u}$  and  $\nabla \vec{u}^T$  the normal and transposed displacement gradients, respectively.

In a stationary situation, the elastic strains  $\hat{\varepsilon}_{el}$  are in equilibrium with stresses inside the cavity walls described by the stress tensor  $\hat{\sigma}$ . Their relation is given by a generalized form of Hooke's law;

$$\hat{\sigma} = \hat{C} : \hat{\varepsilon}_{el} = \hat{C} : (\hat{\varepsilon} - \hat{\varepsilon}_{th}), \quad (2.10)$$

with  $\hat{C}$  a fourth rank stiffness (or elasticity) tensor generally having 21 non-zero components (in case of anisotropic materials). In case of isotropic materials however,  $\hat{C}$  is fully determined by two parameters;  $\hat{C}_{ijkl} = \lambda \delta_{ij} \delta_{kl} + \mu (\delta_{ik} \delta_{jl} + \delta_{il} \delta_{jk})$ , with  $\lambda$  and  $\mu$  the Lamé coefficients which are related to the more familiar Young's modulus  $E$  and Poisson's ratio  $\nu$  by:

$$\lambda = \frac{E\nu}{(1-2\nu)(1+\nu)}, \quad \mu = \frac{E}{2(1+\nu)}. \quad (2.11)$$

The displacement field is finally obtained by determining for each volume element the virtual work done by internal stresses and strains (the internal virtual work;  $\delta W_i$ ) and external forces and displacements (the external virtual work;  $\delta W_e$ ), integrating over the entire domain;

$$\delta W_i = - \int_V \delta \hat{\varepsilon}_{el} : \hat{\sigma} dV, \quad (2.12)$$

$$\delta W_e = \int_S \delta \vec{u} \cdot \vec{F}_S dS + \int_V \delta \vec{u} \cdot \vec{F}_V dV, \quad (2.13)$$

and setting  $\delta W = -\delta W_i - \delta W_e = 0$ . Here,  $\vec{F}_S$ ,  $\vec{F}_V$  are forces acting on the surface and within the volume of the domain. This method is known as the principle of virtual work.

With the displacement field  $\vec{u}$  determined, the geometry can be deformed and used as input for other simulations, such as the third stage simulations mentioned in the previous subsection.

### 2.3.2 Important considerations

In order to keep ourselves from overcomplicating the matter, we have considered simulating only one specific situation up to this point: The one where a stationary stream of electromagnetic energy from an external source flows into a cavity and is dissipated there. Some software packages however, namely Superfish, use internal excitation (as opposed to external excitation).

This can be done by defining a so-called magnetic current (measured in volts), that flows through a fictitious loop inside one of the cells. In case of a 2D axisymmetric simulation, this loop reduces to a single point. It serves as a boundary condition that forces a nonzero solution to the wave equation (and is therefore known as the drive

point). Consequently, since now the cavity has its own wave source, the external source can be modelled using a matched load. Indeed. If we picture a situation where a klystron and a cavity perfectly match the transmission line between them, we see that both klystron and cavity will dissipate half of the total energy, independent of the actual location of the wave source. The only thing that will change if one moves the source from klystron to cavity or back again is the direction of the power flow through the transmission line (in our model, this equals switching between internal and external sources).

The location of the wave source does become important however, when the match between cavity and transmission line is less than perfect (thus creating a bottleneck). Having this bottleneck might seem favourable if the source is placed inside the cavity: The losses are reduced, the quality factor is raised and the same amount of input energy can sustain much stronger fields. The problem here of course, is that this very same bottleneck prevents the input energy from entering the cavity in the first place. To prevent misleading results, the safest approach would be to only consider simulations where the source is placed outside the cavity (as we have done so far). However, since sometimes internal excitation is the only option, we will have to keep in mind the effects of source location and mismatching.

Secondly, we should be aware of the difference between average power and peak power. If we consider our cavity to be a resonant structure accelerator, we will only be interested in its peak power (because during the power peak our electrons will be accelerated). If we consider our cavity to be a heat source on the other hand, we will have to take into account its average power. Or to put it more directly: If we want to simulate fields that will be used to accelerate electrons, we will have to use peak power. If we want to simulate power dissipation, heat transport and deformation, we will have to use average power. After all, it is the average power (and thus, the necessary cooling capacity) that distinguishes high rep-rate cavities from low rep-rate ones.

Lastly, since our goal is to perform a numerical and experimental study of RF-photoguns in general, our simulations should not depend too much on our benchmark setup's intended functioning: Even operating our setup in a completely inappropriate way may turn out to be an excellent means for validating our simulations. For example, if we want our model to include deformations typical for high rep-rate situations, even though our wave source isn't powerful enough to create these situations, we should apply heat in other ways: By using the cavity's cooling channels for instance (by pumping hot coolant). Because our models will have to support situations like these, we will have to add alternative heat sources in the form of extra boundary conditions.



## NUMERICAL STUDY

---

Discovering the ins and outs of resonant structure modelling has proven to be a diverse challenge. This chapter will treat several of its aspects starting with numerical methods (Section 3.1) and optimisations (Section 3.2). We then proceed with basic validation (Section 3.3) and tuning (Section 3.4). The chapter is concluded with some examples (Section 3.5).

### 3.1 NUMERICAL METHODS

One of the tools we have used to benchmark our Comsol simulations is a software package called Poisson Superfish<sup>1</sup>. Comparable to Comsol, Superfish simulates electromagnetic fields inside a cavity using partial differential equations and boundary conditions. Superfish is an interesting benchmark for two reasons: To start with, it has earned its stripes as a reliable resonant structure analysis tool for over three decades (originally written in 1976). Secondly, since it uses a solving method that differs from the one Comsol uses, it allows us to examine the effects of different solving methods on the obtained results.

Instead of using the finite element method, Superfish uses the less advanced finite difference method. The main difference between the two methods is the way discretisation takes place. Whereas the finite element method solves partial differential equations by expanding the total solution in a linear combination of so-called shape functions, the finite difference method solves the partial differential equations by replacing their derivatives with finite differences [5, p. 589-600].

The process of numeric solving can be rather complicated and treating its details is beyond the scope of this text. Even so, since these methods form one of the cornerstones of this work, we have examined their basic principles: A simplified example of both methods solving the heat equation is included as Appendix A.

### 3.2 OPTIMISATIONS

When one moves from a theoretical description of what an outcome should be like to actually calculating the outcome, one will discover hardware and software limitations play an important role: The problem has to be specified in such a way that the used computing system can determine a reasonably accurate solution within a reasonable amount of time.

---

<sup>1</sup> [http://laacg1.lanl.gov/laacg/services/serv\\_codes.phtml](http://laacg1.lanl.gov/laacg/services/serv_codes.phtml)

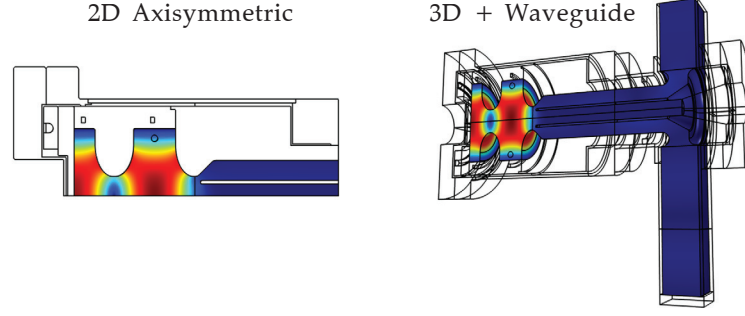


Figure 3.1: The cavity as a 2D or 3D problem.

Our modelling system is equipped with a Core i7-2600 Processor running at 3.40GHz, 16.0GB DDR3 memory at 1333MT/s (21GB/s), and a 250GB SATA hard disk at 7.2Krpm (6.0Gb/s). Additionally, we used Windows 7, 64bit and Comsol 4.2a (4.2.1.166). Using the operating system's own tools, we have monitored the processor and memory activity during simulations. We have found that the amount of memory forms the most important limitation. The performance dramatically decreases as soon as more than 16GB of memory is needed (forcing the system to use the hard drive).

Consequently, we have done most simulations in two dimensions (most notably the thermal expansion ones), by ignoring the rectangular waveguide (Figure 3.1, right) and treating the cavity and coaxial line as an axisymmetric problem (Figure 3.1, left). Some simulations have been developed as 2D-3D hybrids, with stages one and two in two dimensions and stage three in 3D (here, the stages refer to the ones mentioned in Section 2.3).

In order to further improve performance, we have developed a meshing optimisation scheme: To start with, we multiply all mesh spacing parameters by a factor of  $\alpha = 0.5^{\theta/D}$ , with  $\theta$  a mesh tuning parameter and  $D$  the number of dimensions used for the geometry. As a rule of thumb, lowering  $\theta$  by one will half the number of mesh points, the number of degrees of freedom and the amount of memory needed. As an example we have;

$$\begin{aligned}\bar{s}_m(\theta, D) &\propto \{p_m\} \cdot \alpha = \{p_m\} \cdot 0.5^{\theta/D} \\ \therefore \bar{s}_m(\theta - 1, 2) &\propto \{p_m\} \cdot 0.5^{(\theta-1)/2} \\ &= \{p_m\} \cdot 0.5^{\theta/2} \cdot \sqrt{2} \propto \bar{s}_m(\theta, 2) \cdot \sqrt{2},\end{aligned}$$

with  $\bar{s}_m$  the average mesh size and  $\{p_m\}$  a collection of mesh spacing parameters (since  $\bar{s}_m$  also depends on the geometry itself, we have used semi proportionality). However, apart from decreasing the total number of mesh points, lowering  $\theta$  will also decrease the quality of the results. The optimal settings are found by examining the convergence of the results as a function of  $\theta$ .

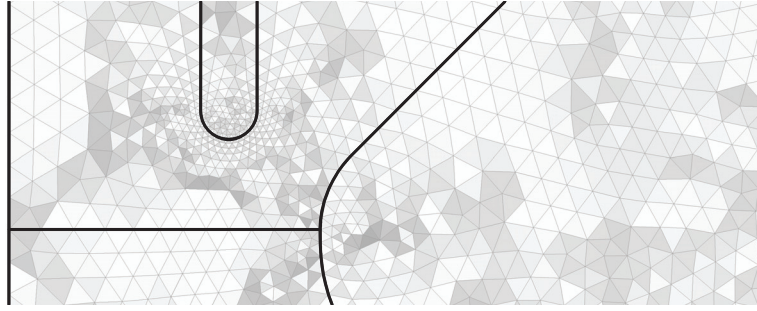


Figure 3.2: The spatial distribution of mesh points in a 2D geometry.

Secondly, we improve the mesh by simplifying the geometry: The spatial distribution of an optimised mesh is mostly based on geometry features (Figure 3.2). The mesh size is increased in large open spaces and reduced near narrow regions and bends. By removing details from the geometry that are not crucial to the outcome of the simulation, the number of mesh points can be reduced by more than thirty per cent. Lastly, we increase the number of mesh points in places where high accuracy is important.

### 3.3 BASIC VALIDATION

Before validating our simulations using detailed temperature and reflection measurements, we will first do some basic validation using existing measurements, cavity theory and Superfish. When working with Superfish, we have to keep in mind that Superfish does not support three dimensional geometries or impedance boundary conditions. Instead, the electromagnetic fields are determined using perfectly conducting walls in two dimensions. Once the field geometry is known, the losses are introduced during a post processing step and field strengths are scaled down accordingly.

This happens to be a pretty good approximation. After all, the difference between good conducting walls and perfectly conducting walls is not that large (the frequency shifts only about 128KHz, or 0.0043%). However, if we want to compare Superfish's results to those from Comsol, we will have to be aware of the implications: In Superfish, the field lines and eigenfrequencies correspond to perfectly conducting walls, whereas other parameters such as the quality factor, shunt impedance and field strength correspond to normally conducting walls.

#### 3.3.1 Eigenfrequency

Since the eigenfrequency is the most characteristic property of a resonant structure, we will use it as our first benchmark criterion. Since Superfish's eigenfrequency corresponds to perfectly conducting walls,

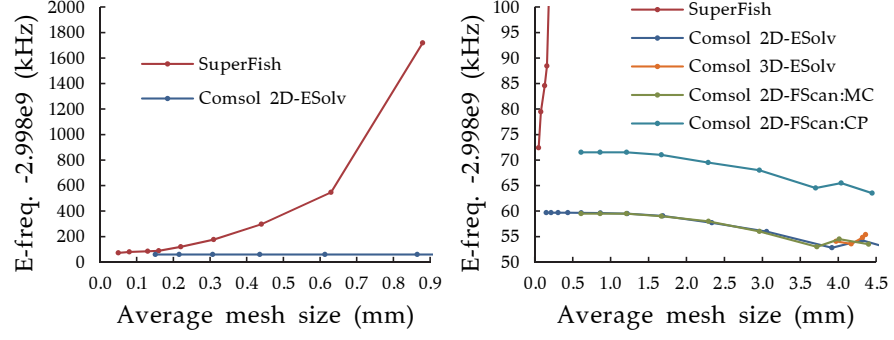


Figure 3.3: Convergence of the eigenfrequency for different solvers.

we use perfectly conducting walls in Comsol as well (normally conducting walls will be introduced later on). The used geometries are based on our setup's design drawings.

- Comsol  $\Leftrightarrow$  Superfish (both eigenvalue solvers, perfect conductor, 2D): Figure 3.3 shows the eigenfrequency as a function of the average mesh size. Superfish starts at 2.999719GHz ( $\bar{s}_m = 0.880\text{mm}$ ) and goes to 2.998072GHz ( $\bar{s}_m = 0.050\text{mm}$ ). It drops 1647KHz when going from 0.880mm to 0.050mm. The last iteration shows a drop of about 7KHz, suggesting the eigenfrequency will continue to drop for values  $\bar{s}_m$  smaller than 0.050mm. A straight line fitted through the last four iterations ( $R^2 = 0.97$ ) suggests an eigenfrequency of 2.998067GHz at  $\bar{s}_m = 0.000\text{mm}$ .

Comsol shows a much more stable convergence pattern. It starts at 2.998052GHz ( $\theta = 0$ ,  $\bar{s}_m = 4.790\text{mm}$ ) and goes to 2.998060GHz ( $\theta = 12$ ,  $\bar{s}_m = 0.151\text{mm}$ ). At  $\theta = 7$  ( $\bar{s}_m = 0.865\text{mm}$ ), the difference with respect to the final value is already below 53Hz. The difference between the last two iterations is less than 6Hz which is on the order of the numerical noise. We see large differences between Superfish and Comsol with respect to convergence behaviour (in favour of Comsol). Their final eigenfrequencies however, are in good agreement.

- Two dimensions  $\Leftrightarrow$  three dimensions (both eigenvalue solvers, perfect conductor, Comsol): Since we have determined that Superfish and Comsol are in agreement, we can move on and compare 2D to 3D (the 3D geometry is a revolved version of the 2D geometry). As a function of average mesh size, the eigenfrequencies seem to be about the same (differences are on the order of 1KHz, figure 3.3). The 2D version starts at 2.998052GHz and arrives at 2.998060GHz (the same convergence pattern as described above). The 3D version does not show a clear convergence pattern, as we couldn't use mesh sizes smaller than 3.973mm (because of limited computing power).

Judging from the convergence pattern of the 2D case and the lack of differences between 2D and 3D, the 3D version would have arrived at 2.998060GHz as well. This means that even though we have never had the processing power to test the 3D version below 3.973mm, we

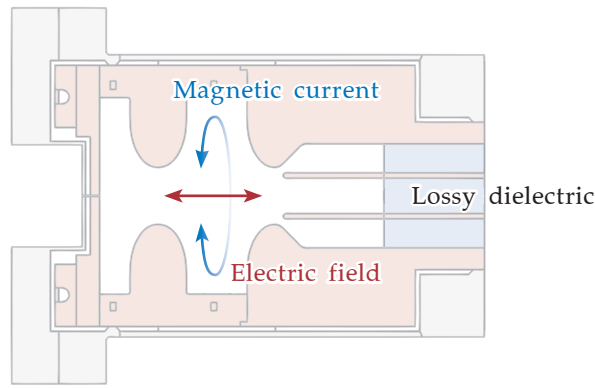


Figure 3.4: The magnetic current and the lossy dielectric.

still can determine our calculated eigenfrequency to be within 6KHz of its final value (the same error estimation can be done for other parameters as well, like  $Q_{ul}$  or  $R_{sh}$  for instance). These findings become important when 3D is the only option i.e. when including the rectangular waveguide.

- Frequency scan: magnetic current  $\Leftrightarrow$  eigenvalue solver (2D, perfect conductor, Comsol): The frequency scan has several advantages when compared to the eigenvalue solver. Whereas the eigenvalue solver can take several hours to complete without giving transparent feedback about its progress, the frequency scan only takes a couple of seconds per frequency and gives a live recording of its heading. Furthermore, the frequency scan doesn't give arbitrary field strengths and often gives a useful response (even in cases that need multi-physics or complex geometries). The frequency scan can be stopped and (re)started at any time and the user may choose frequency intervals and resolutions as he or she wishes.

The magnetic current type frequency scan uses an internal magnetic current to excite the cavity. This magnetic current is measured in volts and flows through a fictitious loop placed inside the right cell (Figure 3.4). It is Comsol's analogue to Superfish's drive point. The eigenfrequency is found by scanning a suitable frequency interval using a resolution of 500Hz, and looking for the frequency that maximises the electromagnetic energy stored inside the cavity. Figure 3.3 shows a perfect correspondence between the magnetic current type frequency scan and the eigenvalue solvers.

- Freq scan: magnetic current  $\Leftrightarrow$  freq scan: coax port (2D, perfect conductor, Comsol): The coax port type frequency scan excites the cavity externally (using the coaxial line). To our surprise, we find a consistent difference of about 12KHz independent of mesh size, between frequency scans that use internal and external excitation (Figure 3.3). This can be explained as follows: When looking at the solvers that use internal excitation, we see that the power flows from the cavity to the end of the coaxial line. In order to keep it from reflecting,

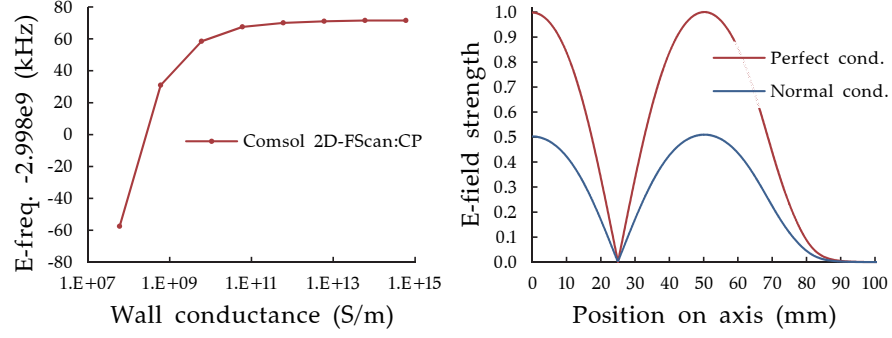


Figure 3.5: Influence of wall conductance on eigenfreq. and electric field.

we should have terminated the coaxial line using a matched load. However, Superfish does not support matched loads.

Instead, we have terminated the coaxial line using a lossy dielectric having  $\epsilon_r = \mu_r = 0.6 + 0.8i$  (in both Superfish and Comsol, [Figure 3.4](#)). Because the magnitudes of  $\epsilon_r$  and  $\mu_r$  are equal to  $\sqrt{0.6^2 + 0.8^2} = 1$ , there will be no reflections at the vacuum to dielectric interface. If the length of the lossy dielectric were infinite, all incoming power would be absorbed (which would make the dielectric effectively the same as a matched load). However, since the length of the dielectric is finite (30mm), a small fraction of the escaping power will return, changing the resonance properties of the cavity.

Indeed. Replacing the dielectric by a matched load resolves the matter (this can be done in Comsol by removing the dielectric and adding a coaxial port that is turned off). Magnetic current and coax port type simulations are now both equipped with a coaxial port (in the coax port case it's turned on). They now both converge to the same eigenfrequency of 2.998072GHz.

### 3.3.2 Wall conductance

We will study the effects of a finite wall conductance using the impedance boundary condition node in Comsol. We start with a wall conductance that approaches infinity (this should reproduce the results we have had so far). After that, we proceed by reducing the conductance to normal values.

- Perfect conductor  $\Leftrightarrow$  normal conductor (2D, frequency scan: coax port, Comsol): [Figure 3.5](#) shows the eigenfrequency as a function of wall conductance (here, we have used external excitation). For conductance values  $\sigma > 10^{12}$  S/m the eigenfrequency stays constant at 2.998072GHz, and drops to 2.997944GHz when  $\sigma$  is reduced to  $5.91 \cdot 10^7$  S/m (the actual conductance of C10100 OFHC Copper). This is in good correspondence to the design frequency of this cavity; 2.99795GHz. Other parameters follow the same pattern: The unloaded quality factor drops from  $11.548 \cdot 10^6$  to  $11.580 \cdot 10^3$ , the shunt-

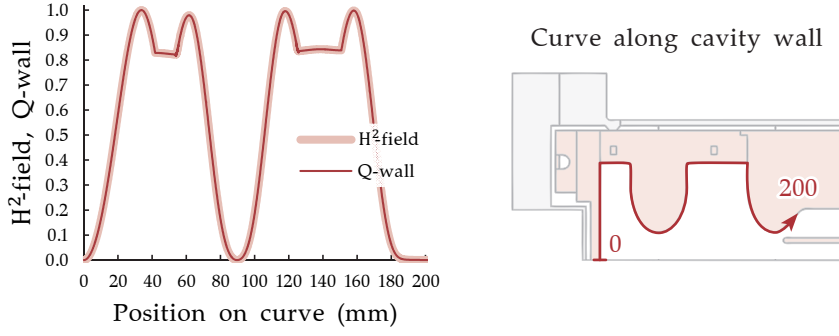


Figure 3.6: Magnetic field and heat production along the wall surface.

impedance drops from  $50.173 \cdot 10^9 \Omega/\text{m}$  to  $50.327 \cdot 10^6 \Omega/\text{m}$  and the phase shift (between the cells) drops from  $180.000^\circ$  to  $177.638^\circ$  (note that this results equals  $2.362^\circ$ ; the design value is  $2.3^\circ$ ).

Additionally, we have examined the field strengths as a function of wall conductance (at constant input power). Figure 3.5 shows us, the on-axis electric field strength drops to about 50% of its original value when going from perfectly conducting walls to normally conducting walls. The top curve represents the fields as determined by all perfect conductor type solvers (in order to compensate for the eigenvalue solver's arbitrary field strengths, these are all normalized to one).

Finally, we have validated dissipation and thermal expansion: We have checked that the distribution of electromagnetic power deposited into the cavity's walls follows the local magnetic field distribution (as the used boundary conditions would suggest). That this is indeed the case, is shown in Figure 3.6. Thermal expansion has been validated by heating the cavity up to a certain point and checking if the acquired expansion corresponds to what one would expect given the thermal expansion coefficients used.

Judging from the nice correspondence and stable convergence of all results up to this point, our basic validation seems to be complete.

### 3.4 TUNING

One of the main points of having a valid model is the ability to maximise performance by optimising various input parameters. In the case of the 1.5-cell TU/e gun, we will examine the geometry's influence on the structure's performance.

As an example, we will vary the position of the antenna (the inner conductor of the coaxial line) and determine if a position closer to or farther from the iris would be preferable. To start with, we will choose a performance criterion: The amount of power needed at resonance to establish field strengths equal to the ones mentioned in the design specifications. More specifically, when looking at the on-axis electric field, we want the average of the two peak heights to be  $110\text{MV/m}$ .



Secondly, we will choose a parameter definition: The distance in millimetres between the antenna's tip and the centre of the right iris.

This illustrates our challenge: For each value of the antenna's position, we first have to find the eigenfrequency and secondly, we have to determine how much power should be applied to get the desired field strengths. The situation gets even more complicated when thermal expansion is included. In that case, the eigenfrequency will not only depend on the parameter's value, but also on the amount of power applied.

Clearly, the methods we have used so far are impractical: The eigenfrequencies have to be picked by hand, the resolutions are 500Hz at best (higher resolutions are possible, but not without increasing the number of iterations beyond unpractical levels) and there is no easy way to determine the amount of power needed. Using these scans to find optima will therefore be an extremely laborious task.

#### 3.4.1 PPF-Scans

Our solution is to combine a coax port type simulation with multi-dimensional scans and polynomial interpolation. To start with, we equipped our simulations with a large number of probes. These allow us to get a maximum insight into the system's reaction to our input parameter. They can be applied to domains, boundaries, edges, points or the system as a whole. They measure the amount of power dissipated, the amount of energy stored, reflections, phase shifts, field strengths, voltage gains, temperatures and many more. Consequently, each separate simulation generates a (large) dataset, stored in a so-called accumulated probe table.

We then proceeded by adding a multidimensional scan (a nested parametric sweep): Comsol will apply several parameter values. For each parameter value, it will apply several power levels and for each power level, it will apply several frequencies (this is why we dubbed it the Parameter-Power-Frequency scan, or PPF-scan for short).

In our example, the input parameter's design value is 3.165mm, at 40°C (as dictated by the TU/e). In our sweep, we will use the interval [3.00, 0.05, 4.00] mm, at 40°C (where the first value is the starting point, the second value is the step size and the third is the stopping point). Additionally, the frequencies and power levels will be [2997890, 30, 2998010] kHz and [2.00, 1.00, 4.00]<sup>2</sup> MW (where we have squared our power levels in order to achieve a linear increase in field strength). Comsol will iterate through 21 parameter values, 3 power levels and 5 frequencies, creating a collection of 315 datasets;

$$\mathcal{D} \equiv \left\{ \vec{D} \in \mathbb{C}^n : \vec{D}(x_i, p_j, f_k) = [d_1(x_i, p_j, f_k), \dots, d_{n-1}(x_i, p_j, f_k), d_n(x_i, p_j, f_k)]^T, \quad \forall x_i, p_j, f_k \right\},$$



where  $i, j, k$  are integers,  $x_i, p_j, f_k$  are the used PPF-values,  $d$  is the probe data and  $n$  is the total number of probes. Once these datasets have been created, they will be exported into a PPF-script, that puts them in a three dimensional array (having dimensions  $21 \times 3 \times 5$ ). The main goal of this script is to collapse the dimensions, leaving us with one single dataset (note that we will need orthogonality here; the PPF-values shouldn't be dependent on one another). This dataset will then contain all the information that we would have obtained, had we done the simulation using the optimum antenna position and the correct amount of power, at resonance.

We start by collapsing the frequency dimension. From cavity theory, we know the relation between the angular frequency and the electromagnetic energy stored inside the cavity to be

$$U \propto \frac{1}{(\omega - \omega^0)^2 + (\omega^0/2Q)^2}, \quad (3.1)$$

with  $\omega^0$  the angular eigenfrequency and  $Q$  the quality factor of the cavity [2, p. 357]. When  $\delta\omega = \omega - \omega^0$  approaches zero, we have

$$\lim_{\delta\omega \rightarrow 0} U \propto \frac{1}{(\omega^0/2Q)^2} - \frac{(\omega - \omega^0)^2}{(\omega^0/2Q)^4}, \quad (3.2)$$

i.e. close to the eigenfrequency  $U(\omega)$  can be approximated by a parabola (and its derivative by a straight line).

This allows the PPF-script to find the  $21 \times 3$  eigenfrequencies: It iterates through all used parameter-power combinations;  $x_i, p_j$ . For each combination, it checks all used frequencies  $f_k$  and picks the one (that we will label  $f_0$ ) that has the largest energy stored value in its dataset. Then, it uses finite differences;

$$\begin{aligned} f_{-\frac{1}{2}} &= \frac{1}{2} (f_0 + f_{-1}), & f_{+\frac{1}{2}} &= \frac{1}{2} (f_{+1} + f_0), \\ \Delta U_{-\frac{1}{2}} &= U(f_0) - U(f_{-1}), & \Delta U_{+\frac{1}{2}} &= U(f_{+1}) - U(f_0), \end{aligned}$$

and first order polynomial interpolation (Figure 3.7);

$$f_e = f_{-\frac{1}{2}} \frac{\Delta U_{+\frac{1}{2}}}{\Delta U_{+\frac{1}{2}} - \Delta U_{-\frac{1}{2}}} + f_{+\frac{1}{2}} \frac{\Delta U_{-\frac{1}{2}}}{\Delta U_{-\frac{1}{2}} - \Delta U_{+\frac{1}{2}}}, \quad \forall x_i, p_j,$$

where  $f_{-1}$  and  $f_{+1}$  are the previous and next frequencies respectively,  $U(f_k)$  is the energy stored value in the dataset of  $f_k$  and  $f_e$  is the to-be-determined eigenfrequency. There is one value  $f_e$  for each parameter-power combination i.e.  $f_e = f_e(x_i, p_j)$ . Tests have shown that even for frequency resolutions of  $f_k - f_{k-1} = 30\text{kHz}$ , the accuracy of  $f_e$  is  $< 75\text{Hz}$ . This is on the order of the accuracy of the simulations themselves (assuming a mesh parameter of  $\theta = 6$  is used).

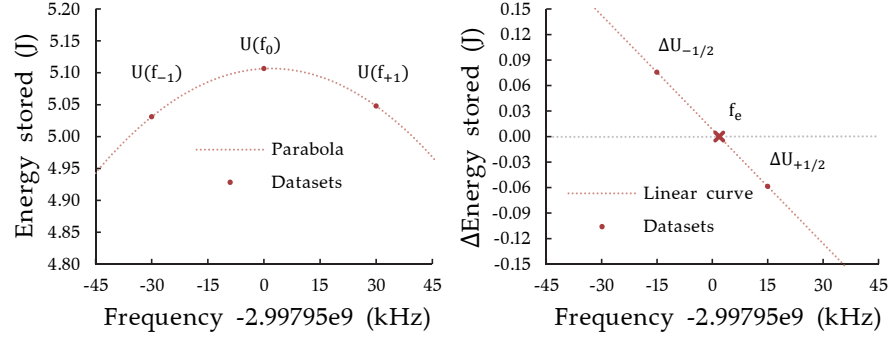


Figure 3.7: Use of first order polynomial interpolation to find  $f_e$ .

The datasets corresponding to the eigenfrequencies,  $\vec{D}(x_i, p_j, f_e)$ , are obtained by assuming all probe data shows a second order dependency on  $f$  at most i.e.  $d_m(f) \in \mathbb{P}_2, \forall m$ . This allows us to use polynomial interpolation once more;

$$\vec{D}(f_e) = \vec{D}(f_{-1}) \cdot L_{-1}(f_e) + \vec{D}(f_0) \cdot L_0(f_e) + \vec{D}(f_{+1}) \cdot L_{+1}(f_e),$$

for all  $x_i, p_j$ , where  $L_{-1}(f)$ ,  $L_0(f)$  and  $L_{+1}(f)$  are the second order interpolating Lagrange polynomials corresponding to the nodes  $f_{-1}$ ,  $f_0$  and  $f_{+1}$  (that is;  $L_k(f_k) = 1, L_k(f_l) = 0, \forall k, l, l \neq k$ ). For frequency resolutions of  $f_k - f_{k-1} = 30\text{kHz}$ , the acquired values  $d_m(f_e)$  were tested to be off by about  $1 \cdot 10^{-2}$  to  $1 \cdot 10^{-6}\%$ , when compared to the values determined by a simulation actually running at  $f_e$ .

Now, by replacing the dataset collections  $\vec{D}(f_k)$  by the single datasets  $\vec{D}(f_e)$  for all values of  $x_i$  and  $p_j$ , we have effectively collapsed the frequency dimension:

$$\vec{D}(x_i, p_j, f_e) = \vec{D}(x_i, p_j, f_e(x_i, p_j)) = \vec{D}(x_i, p_j), \quad \forall x_i, p_j.$$

In order to collapse the power dimension, we use  $P \propto |E|^2$ : The script iterates through all used parameter values. For each value, it checks all used power levels  $p_j$  and picks the one (that we will label  $p_0$ ) that has the electric field peaks closest to 110MV/m. Then, it determines the average peak heights for  $p_{-1}$ ,  $p_0$ , and  $p_{+1}$ ;

$$\begin{aligned} \bar{E}_{-1} &= \frac{1}{2} (E^1(p_{-1}) + E^2(p_{-1})), \\ \bar{E}_0 &= \frac{1}{2} (E^1(p_0) + E^2(p_0)), \\ \bar{E}_{+1} &= \frac{1}{2} (E^1(p_{+1}) + E^2(p_{+1})), \quad \forall x_i, \end{aligned}$$

with  $p_{-1}$  and  $p_{+1}$  the previous and next power levels respectively and  $E^1(p_j), E^2(p_j)$  the two electric field peak values in the dataset of  $p_j$ . The correct power levels are then determined by setting the value  $\bar{E}_c = 110\text{MV/m}$  and using second order polynomial interpolation;

$$p_c = p_{-1} \cdot \mathcal{L}_{-1}(\bar{E}_c) + p_0 \cdot \mathcal{L}_0(\bar{E}_c) + p_{+1} \cdot \mathcal{L}_{+1}(\bar{E}_c), \quad \forall x_i,$$

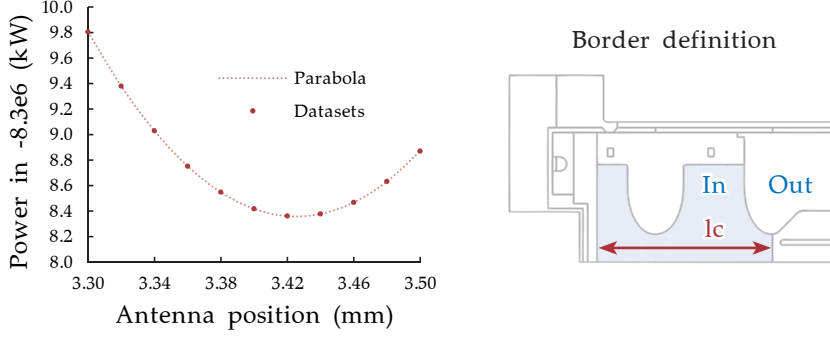


Figure 3.8: Minimum in applied power, PPF-dataset border definition.

with  $p_c$  the to-be-determined power level and  $\mathcal{L}_{-1}(\bar{E})$ ,  $\mathcal{L}_0(\bar{E})$ ,  $\mathcal{L}_{+1}(\bar{E})$  the second order interpolating Lagrange polynomials corresponding to the nodes  $\bar{E}_{-1}$ ,  $\bar{E}_0$  and  $\bar{E}_{+1}$ . There is one value  $p_c$  for each parameter value i.e.  $p_c = p_c(x_i)$ .

The datasets for the correct power levels,  $\vec{D}(x_i, p_c)$ , are obtained in the same way as for  $\vec{D}(x_i, p_j, f_e)$ , but with one important difference: Some of our probe data shows a half order dependency on  $p$  that is;  $d_m(p) \propto \sqrt{p}$ , preventing a proper second order polynomial fit. This is solved by a variable transformation: When using the nodes  $\sqrt{p_j}$  in the Lagrange polynomials instead of  $p_j$ , root functions will change into first order ones and first order functions will change into second order ones, allowing second order interpolation nonetheless;

$$\vec{D}(p_c) = \vec{D}(p_{-1}) \cdot \mathcal{L}_{-1}(\sqrt{p_c}) + \vec{D}(p_0) \cdot \mathcal{L}_0(\sqrt{p_c}) + \vec{D}(p_{+1}) \cdot \mathcal{L}_{+1}(\sqrt{p_c}),$$

for all  $x_i$ , with  $\mathcal{L}_{-1}(\sqrt{p})$ ,  $\mathcal{L}_0(\sqrt{p})$  and  $\mathcal{L}_{+1}(\sqrt{p})$  the Lagrange polynomials corresponding to the nodes  $\sqrt{p_{-1}}$ ,  $\sqrt{p_0}$  and  $\sqrt{p_{+1}}$ . As before, this allows us to collapse a dimension;

$$\vec{D}(x_i, p_c) = \vec{D}(x_i, p_c(x_i)) = \vec{D}(x_i), \quad \forall x_i,$$

leaving 21 datasets (one for each parameter value). These allow us to plot probe data as a function of  $x$ ;  $d_m(x)$ .

Finally, we may choose to collapse the last dimension as well. The most straightforward way to do this is to find the smallest amount of power needed to maintain the required field strength;

$$P(x_i) < P(x_j), \quad \forall j, \quad j \neq i,$$

and use finite differences and polynomial interpolation once more (in case  $P$  is applied using the coax port and  $x$  refers to the antenna position,  $P(x)$  tends to resemble a parabola; Figure 3.8). The result is one dataset  $\vec{D}(x_c, p_c, f_e)$  containing all probe data for a single, but optimal situation.

	TU / E VALUES	DEFAULT	OPTIMUM
$T(^{\circ}\text{C})$	40	40.00	40.00
$x(\text{mm})$	3.165	3.165	3.425
$f_e(\text{GHz})$	2.99795	2.997944	2.997952
$\Gamma_{dB}(\text{dB})$	—	−29.869	−41.788
$\varphi_{sh}(^{\circ})$	2.3	2.362	2.357
$P_{in}(\text{MW})$	8.5	8.315	8.308
$P_{loss}(\text{MW})$	8.5	8.301	8.303
$E_{st}(\text{J})$	5.0	5.103	5.107
$E_{pl}(\text{MV/m})$	110	109.060	108.953
$E_{pr}(\text{MV/m})$	110	110.940	111.047
$E_{pw}(\text{MV/m})$	100	100.807	100.905
$U_0(\text{MV})$	—	5.599	5.600
$Q_{ul}$	11278	11580.266	11585.469
$R_{sh}(\text{M}\Omega/\text{m})$	—	50.327	50.343
$R_{sh}/Q_{ul}(\text{k}\Omega/\text{m})$	—	4.346	4.345

Table 3.1: PPF-scan results compared to values provided by the TU/e.

$T$	Temperature of the cavity.
$x$	Position of the antenna.
$f_e$	Eigenfrequency of the cavity.
$\Gamma_{dB}$	Power reflected back into the coaxial line.
$\varphi_{sh}$	Phase shift between the cells.
$P_{in}$	Power inserted into the coaxial line.
$P_{loss}$	Power dissipated inside the cavity.
$E_{st}$	Energy stored inside the cavity.
$E_{pl}$	Maximum on-axis field strength in the left cell.
$E_{pr}$	Maximum on-axis field strength in the right cell.
$E_{pw}$	Maximum field strength at the left iris surface.
$U_0$	Total voltage gain.
$Q_{ul}$	Unloaded quality factor.
$R_{sh}$	Shunt impedance.

### 3.4.2 Results

The optimum antenna position turns out to be  $x_c = 3.425\text{mm}$ . The resulting dataset is listed in [Table 3.1](#) (rightmost column), together with results from simulations using default settings (the antenna's default position, its design value is  $3.165\text{mm}$ , at  $40^\circ\text{C}$ ) and results from simulations done during the gun's design process (as provided by our TU/e colleagues).

The cavity-coax border used to obtain these values has been defined to be at the centre of the right iris ([Figure 3.8](#)). Apart from defining what readings are from in- or outside the cavity, it sets the length of the integration path used for  $U_0$  and  $R_{sh}$ . As can be seen, our values are in fairly good agreement with the ones used in the TU/e design. Moving the antenna from  $3.165\text{mm}$  to  $3.425\text{mm}$  leads to a small but significant improvement.

### 3.4.3 Discussion

Finally, even though the PPF-scan already achieves significant improvements performance-wise, it is often worth the effort to look for ways to reduce the computational costs even further. For example, in order to obtain the results mentioned above, we should have included expansion, but we didn't. Instead, we utilised the fact that this specific cavity (the one in our test setup) is designed for very low rep-rates (about  $3\text{Hz}$ ). During operation it is supposed to be kept at a constant, uniform temperature of  $40^\circ\text{C}$ , independent of antenna position, peak power, average power or frequency. This allows us to use the original design drawings, scaled up to  $1 + \alpha\Delta T = 1.000338$  (with  $\alpha$  the thermal expansion coefficient and  $\Delta T$  the difference between fabrication and operating temperature;  $20^\circ\text{C}$ ).

We used this approximation primarily because we know expansion simulations to be quite costly (even without scans). Moreover, having no expansion means having no power level dependent eigenfrequencies either (for each  $x_i$ , our PPF-script may use the same  $f_e$  for all  $p_j$ ). It also means having no higher order effects in the relation  $P \propto |E|^2$ , which allows us to test one single value  $P$ , check  $|E|$ , and use the relation  $P \propto |E|^2$  to scale up or down accordingly. Besides, once the values  $x_c$ ,  $p_c$  and  $f_e$  have been obtained, it is a fairly easy task to include expansion still and check if the assumptions were correct. If not, at least we have a fairly good first approximation.

All in all, expansion can often be excluded from low rep-rate simulations (which should not have come as a surprise). Even so, we have included the expansion option in our simulations as well as our PPF-scan algorithms. After all, our goal is to develop simulations that support low rep-rate studies as well as high rep-rate ones.

### 3.5 EXAMPLES

During this project we have done many simulations, most of them have not been discussed here. We have included several of these simulations in [Appendix B](#).

## EXPERIMENTAL STUDY

This chapter starts by describing the setup on which all measurements have been performed (Section 4.1). We then proceed by treating some measurements specifically, starting with temperature gradient measurements (Section 4.2). The chapter concludes with RF-reflection measurements (Section 4.3) and phase thermostration (Section 4.4).

### 4.1 SETUP

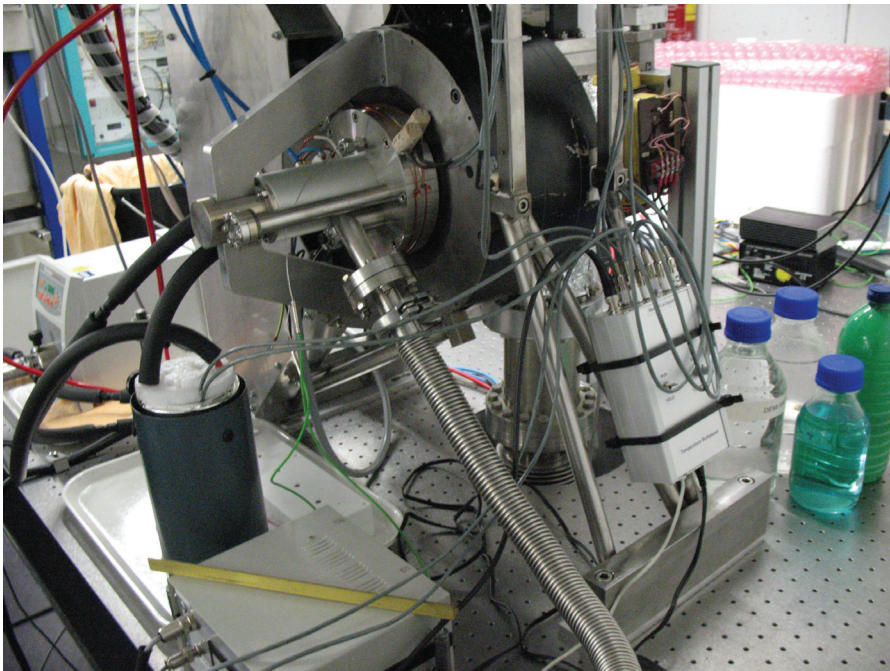


Figure 4.1: Photo of the TU/e 1.5-cell S-band gun.

The setup primarily consists of a six year old normal conducting low rep-rate 1.5-cell 2.998GHz S-band gun from the Eindhoven University of Technology (Figure 4.1). Since its beam line has been dismantled for years and since it has not been properly trained for years either (due to discharges occurring inside the cavity and waveguides, we have not been able to feed more than about 1MW of electromagnetic power into the cavity), we have chosen to decouple the klystron and connect the rectangular waveguide to a network analyser. Furthermore, we have restored and improved its temperature control systems and designed and installed a multichannel thermometer.

Although the setup in its present state cannot produce an electron beam (it has no klystron, no active bucking coil or solenoid, no ex-

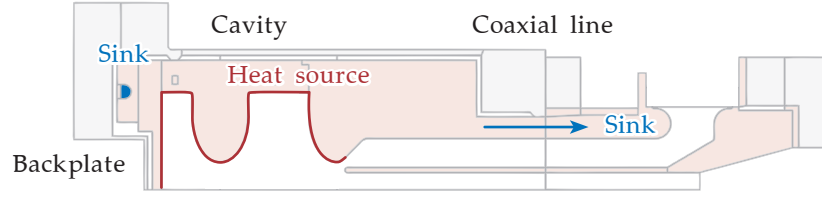


Figure 4.2: Location of the photogun's heat sources and sinks.

citation laser and no beam line), we have performed several fruitful experiments. After all, our goal isn't to accelerate electrons; our goal is to validate our models. This gives us some freedom to improvise: During the experiments we have used the temperature control systems to establish several well-defined temperatures and temperature gradients, while examining the cavity's temperature distribution and resonance behaviour. The results have been used to benchmark our analytical and numerical models.

#### 4.1.1 Network analyser

The electromagnetic properties of the system have been studied using the Rohde & Schwarz ZVH8 cable and antenna analyser. This network analyser applies small amounts of electromagnetic power and measures the cavity's reflection as a function of frequency. In order to get realistic operating conditions, we have put the cavity under the same vacuum as used during particle acceleration ( $\approx 10^{-9}$  mbar).

#### 4.1.2 Temperature control

First, we will briefly describe the existing temperature control systems (the modifications that we added in order to perform our experimental studies are introduced later on): Under normal operating conditions, 75W of electromagnetic energy is dissipated in the cavity (on average). Since the cavity is mounted inside a vacuum chamber, its thermal insulation is rather good in the radial direction. In the longitudinal direction however, there are two main heat sinks; one at the backplate and one near the coaxial line (Figure 4.2).

At the backplate (near the cathode) a cooling ring has been mounted with a 6mm diameter cooling channel. Through this channel coolant (demineralised water) is pumped by a gear pump with a flow rate of about 3l/min ensuring turbulent heat transmission (Reynolds number is on the order of  $10^5$ ). Outside the photogun, the coolant is fed through a 175W Peltier system that can add or remove heat as needed. A Proportional-Integral (PI) controller connected to one of the thermocouples mounted in the cavity wall regulates the Peltier system's power supply. It is able to keep the temperature inside the cavity constant within  $0.05^\circ\text{C}$ .



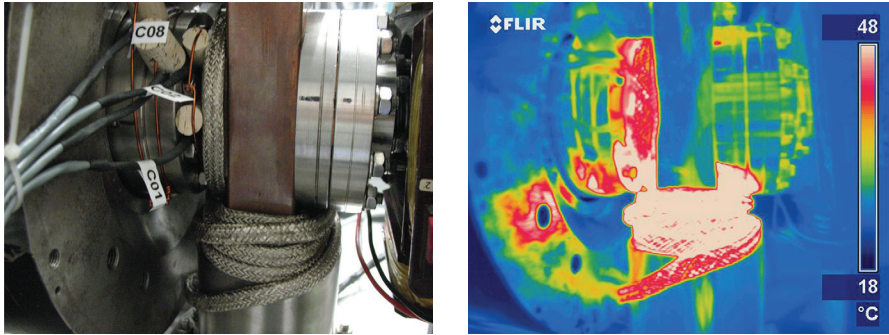


Figure 4.3: Normal and thermal image of the used heating wire.

At the other side (near the coaxial line) however, no cooling or heating elements have been installed. The cavity is clamped directly onto a copper waveguide resulting in good thermal contact between the cavity and the setup's environment (we have confirmed this using temperature probes and a thermal camera). On this side, blowing or walking by easily causes temperature variations of about  $0.5^{\circ}\text{C}$  or more (normally this does not have to be a problem since the area is evacuated during operation).

Now (returning to the present situation), in order to control the temperature near the backplate, we have modified the already installed PI-controlled system by replacing its wall-mounted thermocouple with one placed inside the coolant reservoir. This way, the two thermocouples in the cavity wall both become available for temperature measurements. Admittedly, it also causes the system to have a shorter reaction time since the cavity's heat capacity has been removed from the feedback loop. This however, has had no consequences for our experiments.

Realising accurate temperature control near the coaxial line has been less obvious: We have wrapped a heating wire (normally used during bake-out) around the waveguide (Figure 4.3) and added some insulation. The heating wire is connected to a variable power supply, allowing us to manually control the applied heat. Not surprisingly, since there is no feedback loop of some sort, typical times needed to reach stable temperatures (within  $0.05^{\circ}\text{C}$ ) are on the order of 4-6 hours (with regular monitoring and manual feedback). Nevertheless, when combined with the PI controller, this allowed for rather precise temperature control on both sides of the photogun.

#### 4.1.3 Multichannel thermometer

Initially, the photogun was equipped with two temperature probes (two thermocouples mounted inside the cavity wall). However, two probes are not sufficient to test our numerical models. Since our heat simulations need several realistic Dirichlet boundary conditions

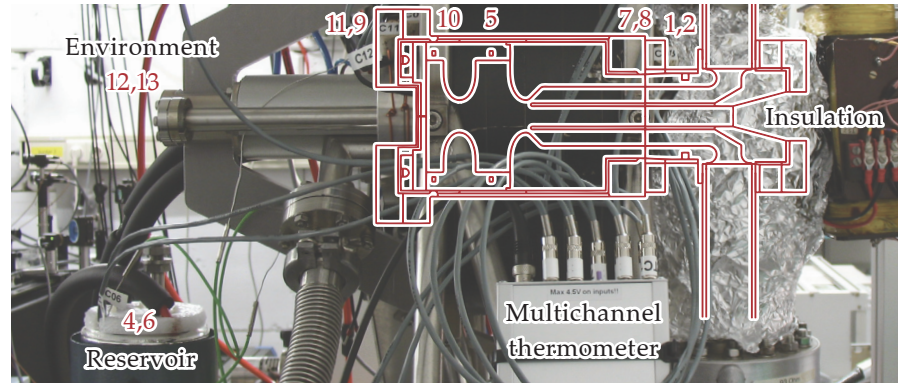


Figure 4.4: Location of the used temperature sensors.

(boundaries with known temperature), we need multiple simultaneous temperature measurements.

This creates the need for an accurate multichannel thermometer: The sensors we have used are of the semiconductor type; LM35-DZ. We've chosen LM35 sensors since they are cheap and easy to install, have high output levels proportional to temperature (no amplification needed) and do not require cold junction compensation (as opposed to thermocouples). In order to compensate for their disadvantages (low accuracy and sometimes, instability) we have carefully calibrated them (increasing relative accuracy from  $\pm 3^\circ\text{C}$  to  $\pm 0.01^\circ\text{C}$ ) and applied redundancy (using them in pairs). More details on the multichannel thermometer are included as [Appendix C](#).

#### 4.2 TEMPERATURE GRADIENT MEASUREMENTS

In order to study the thermal behaviour of the system, we have subjected the cavity to several heat gradients (in the longitudinal direction). These gradients have been applied by fixing the backplate temperature of the photogun significantly above or below the environment's temperature and waiting for the coaxial line temperature to become stationary as well (we have not used the heating wire).



Figure 4.5: Two LM35 sensors clamped against a steel flange (Ch9, 11).

#### 4.2.1 *Measuring*

Measuring the resulting temperatures is done using the multichannel thermometer. A total of 12 channels has been used; 2 internal (the two thermocouples) and 10 external (the LM35 sensors, [Figure 4.4](#)):

- 0 Reference channel (used to identify the other channels).
- 1,2 Coaxial line; surface (copper).
- 3 Not used (unstable).
- 4,6 Reservoir; coolant (demi water).
- 5,10 Cavity wall; thermocouples (right, left cell, copper).
- 7,8 Flange; coaxial line, surface (left, right flange, steel).
- 9,11 Flange; backplate, surface (right, left flange, steel).
- 12,13 Environment (solenoid surface; steel, ring; copper).
- 14,15 Not used (unstable, vacant).

Channels 1,2,7,8,9,11 are all connected to LM35 sensors clamped against the photogun's outer surface ([Figure 4.5](#)). In order to increase thermal contact with the surface and minimise thermal contact with the environment, thermal paste and cork is used. Channels 12,13 are clamped against surfaces as well, but without insulation (they are intended to measure the temperature of the setup's environment, the lab temperature). Channels 4,6 are connected to LM35 sensors submerged in coolant. The coolant is kept turbulent by a flow rate of about 3l/min and insulated from the environment (all tubing has been insulated and a thermos bottle is used as a reservoir, leakage has been checked using a thermal camera). The remaining channels (5,10) are connected to the cavity's thermocouples.

We have applied two gradients, with coolant temperatures of 1.25°C, 47.55°C and coaxial line temperatures of 10.97°C, 36.70°C. We have waited until these temperatures became fairly stable ( $\Delta T < 0.15^\circ\text{C}$  in 5 minutes), and taken data for over 6 minutes at a sampling rate of about 0.42Hz. In order to reduce noise, a Gaussian-shaped moving average with a standard deviation of 60 seconds has been applied during post processing. The averaged value of measurement 75 (exactly halfway the 6 minutes measuring interval) is listed as the final result. Since temperature differences between channels are rather large (order of 10°C), we have chosen  $\pm 0.05^\circ\text{C}$  as our expected measurement error (as explained in [Appendix C](#)).

#### 4.2.2 *Modelling*

In our thermal simulations, we have used the measurements from channel 2 (copper), 6 (coolant) and 7,8,9 (steel) as boundary conditions ([Figure 4.6](#)), and determined the temperature values of both thermocouples. The measured and simulated values are shown in

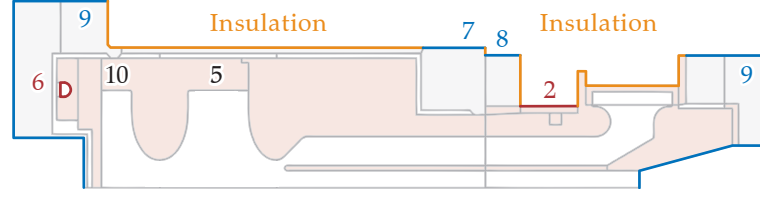


Figure 4.6: Temperatures applied as boundary conditions in thermal model.

**Figure 4.7.** As can be seen, the measured thermocouple values are significantly closer than simulated ( $\Delta T_{5,10} = 0.37^\circ\text{C}$  instead of  $1.71^\circ\text{C}$ ). It thus appears we have used unrealistic parameters for the cavity's thermal resistance (assuming the used equations and solving methods are valid).

Indeed. While the material between the two thermocouples contains practically no interfaces (resulting in direct thermal contact;  $\Delta T_{5,10} \propto Qx_1/k_1$ , with  $x_1$  the distance and  $k_1$  the thermal conductivity), the material between the thermocouples and LM35 sensors actually contains several:  $\Delta T_{2,5} \propto Q(x_1/k_1 + 1/h_1 + x_2/k_2 + 1/h_2 + \dots)$ , where  $h_1$  and  $h_2$  are heat transfer coefficients. Since we have neglected  $h_1$ ,  $h_2$ ,  $\dots$  in our model, our simulated values for  $\Delta T_{2,5}$  and  $\Delta T_{6,10}$  have become too small, making  $\Delta T_{5,10}$  too large.

#### 4.2.3 Discussion

What this experiment tells us is that, using our current setup, we are not able to determine what is actually going on inside our photogun (heat-wise that is); there is too little data and too much unknown.

Admittedly, we could have acquired estimates for heat transfer coefficients from literature, but this would still have left us with the problem that we are unable to accurately verify them. The main problem here, is that the material between our measuring points contains several interfaces. Since these interfaces are placed in series, we are unable to determine how much each interface contributes to the total measured temperature gradient. Besides, we are left with several other issues as well:

- **Too much detail:** In our setup, axial symmetry has been broken in many ways; the cavity's walls are full of holes (in the longitudinal direction). We have not been able to determine how this influences the heat distribution, since 3D models containing such detail would have required far too much computational power.
- **Direction:** In our setup, we have applied heat gradients in the longitudinal direction. In existing high rep-rate designs however, heat primarily flows in the radial direction. This is important since the heat crosses different interfaces in this direction (the materials might be isotropic, the geometry is not).

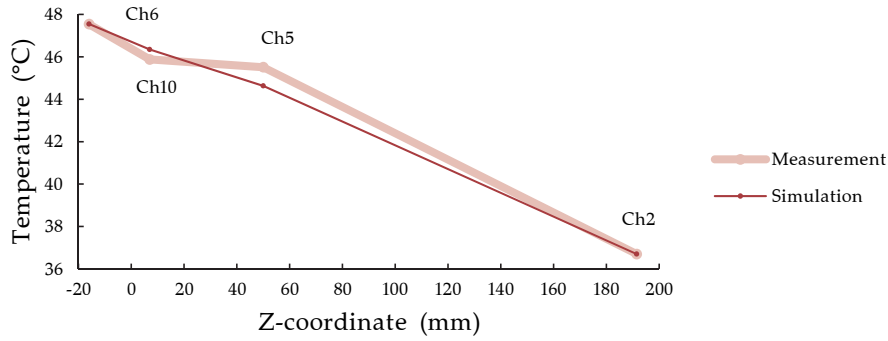


Figure 4.7: Measured and simulated temperature values compared.

- **Interface related issues:** To start with, the cavity parts are clamped together. We have not been able to determine how clamping pressure influences heat transfer. Additionally, there is a coolant-copper interface. We have not been able to determine the roughness or cleanliness of the cooling channel allowing us to use heat transfer coefficients from literature, and we have not been able to measure the heat transfer coefficient directly.
- **Sensor attachment:** The sensors at channels 1,2 have been calibrated simultaneously and attached side by side on the same copper surface. They have not shown any signs of instability. When the surface reaches temperatures significantly above or below the temperature of the environment however, their readings start to differ (up to  $\Delta T_{1,2} \approx 0.4^\circ\text{C}$ , this is why we have used channel 2 in our models; its readings have always been closest to those from channel 6). The reason for this is probably just an incorrect attached sensor at channel 1 (the sensors at channels 1,2 are attached under difficult conditions), but since we cannot be absolutely sure of this, we have chosen to raise the error estimate for all LM35 sensors clamped to the outer surface (to  $\pm 0.2^\circ\text{C}$ , not for temperature stability of course; just for the temperature reading itself).

Considering all of the above, we recommend using numerical as well as experimental prototypes during the development stages of high rep-rate photoguns. Although we have every reason to believe the equations and solving methods used in numerical models are valid, we are not convinced this is enough to ensure reliable results. For example; in some areas, heat fluxes inside a high rep-rate cavity's wall may approach  $10^8\text{W/m}^2$ . When heat fluxes are that large, even small errors in the heat transfer coefficients  $h$  are enough to spoil simulation results (that is;  $\Delta T \propto Q/\delta h$ ).

In cases like these, numerical prototypes shouldn't be seen as a substitute for experimental ones; they should be seen as an extension (note that these prototypes do not necessarily have to resemble the end result, they just should allow for validation).



	Ch2°C	Ch5°C	Ch6°C	Ch10°C	$\Delta T_s^\circ\text{C}$	$\Delta T_{2,6}^\circ\text{C}$	$\Delta t$ min
1	22.47	22.47	22.48	22.47	$\pm 0.01$	0.01	27
2	45.07	45.06	45.03	45.05	$\pm 0.02$	0.04	19
3	22.52	22.53	22.53	22.52	$\pm 0.01$	0.01	16
4	45.04	45.00	45.00	45.01	$\pm 0.01$	0.04	10
5	37.61	37.57	37.54	37.56	$\pm 0.02$	0.07	7
6	29.94	30.04	30.08	30.06	$\pm 0.02$	0.14	8

Table 4.1: Temperatures measured during the reflection experiments.

### 4.3 REFLECTION MEASUREMENTS

The electromagnetic properties of the system (in relation to heat) has been studied by examining its resonance behaviour at different constant temperatures using measurements and simulations. These temperatures have been applied using the PI controller and the heating wire. We have not applied any temperature gradients, since these are difficult to simulate accurately (see discussion in the previous subsection; [Section 4.2.3](#)).

#### 4.3.1 Measuring

Measuring the resulting temperatures is done using our multichannel thermometer (the sensor configuration is the same as for the temperature gradient measurements; [Section 4.2.1](#)). In order to determine the resonance behaviour, frequency scans have been applied (we measured the magnitude and phase of the cavity's reflection). We used the following settings:

Device:	Rohde & Schwarz ZVH8 cable, antenna analyser.
Mode:	Network analyser (measure reflections; $S_{11}$ ).
Centre:	2.995GHz (centre of interval).
Span:	10MHz (length of interval).
Band width:	10kHz (band width of a single measurement).
No points:	1201 (number of measurements in interval).
Trace mode:	Average, 10 (moving average of 10 measurements).

In total, we have done 6 measurements, at 4 temperatures (in increments of  $7.5^\circ\text{C}$ ; about 22.5, 30.0, 37.5 and  $45.0^\circ\text{C}$ ). The temperature at the backplate reached fairly stable values after about 2 hours ( $\Delta T < 0.01^\circ\text{C}$  in 10 minutes). The temperatures near the coaxial line however, took a bit longer (about 4-6 hours), and were less stable;  $\Delta T < 0.02^\circ\text{C}$  in 10 minutes.

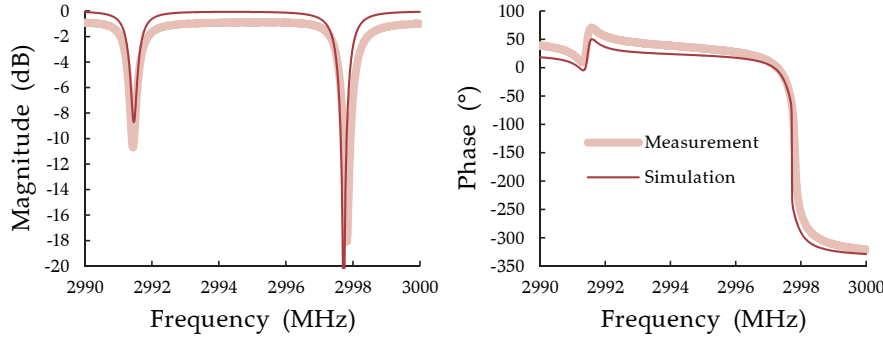


Figure 4.8: Comparison of measurement and simulation (no correction).

The temperature measurements have been done the same way as in [Section 4.2.1](#), but with different timing and accuracy: Instead of picking measurement 75, we've picked measurements done around the same time as our frequency scans (exact timing hasn't been possible, but given the achieved temperature stabilities this should not be a problem). As for the accuracy; we have chosen  $\pm 0.2^\circ\text{C}$  for the LM35 sensors clamped to the outer surface (see discussion in the previous subsection, [Section 4.2.3](#)),  $\pm 0.05^\circ\text{C}$  for the thermocouples and  $\pm 0.01^\circ\text{C}$  for the other sensors (as explained in [Appendix C](#)).

The measurement results from our most relevant channels are listed in [Table 4.1](#). Here,  $\Delta T_s$  refers to the temperature stability (within 10 minutes),  $\Delta T_{2,6}$  refers to the total temperature gradient (between channels 2,6) and  $\Delta t$  refers to the time discrepancy in minutes between temperature measurement and frequency scan (note that we have tested reproducibility as well; the measurements 3,4 were done three weeks later than 1,2). The corresponding results from the frequency scans are listed in the next subsection; [Table 4.2](#).

#### 4.3.2 Modelling

Like before, we have used the measurements from channel 2 (copper), 6 (coolant) and 7,8,9 (steel) as boundary conditions in our thermal simulations (this time, the values of channel 2,6 were about the same and heat flows through the cavity walls were minimal). The temperature distribution that formed has been used to determine the geometry's expansion (second stage). The expanded geometry is used in electromagnetic wave simulations (third stage). The resulting resonance behaviour is shown in [Figure 4.8](#), together with an actual measurement from our network analyser.

Although the general behaviour is reproduced rather well, the depicted curves do not match, suggesting differences between model and measurement. How large these differences are however (and whether they're within specifications), remains less clear. In order to solve this problem, we have fitted our models to the measurements:

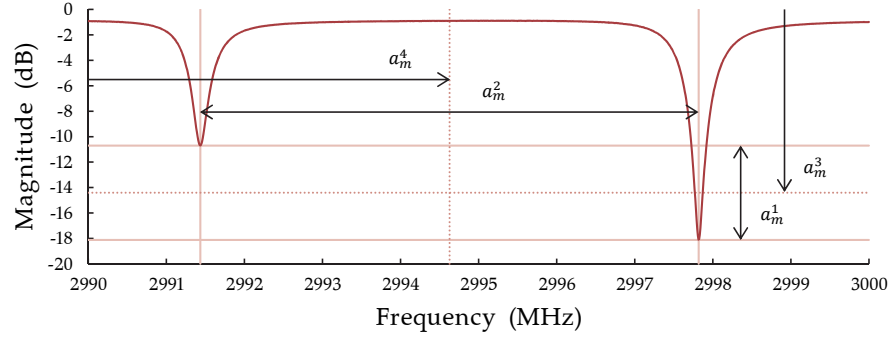


Figure 4.9: The four parameters of the absorption spectrum.

The corrections needed to achieve this have allowed us to get an indication of the differences between measurement and simulation.

To start with, there are several corrections that can be applied without correcting the model itself. For instance; without losing validity, the phase curve can be shifted up and down (the zero-point is arbitrary) and an extra slope can be added to it (which is equivalent to elongating the optical path length; we added about 1.4m). The magnitude curve is shifted down with 0.9dB. This seems reasonable since the simulations exclude several parts of the experimental setup, situated between the cavity and the measurement point (the network analyser's antenna or the RF window for instance).

However, once these corrections were applied, there were still some differences left. In order to minimise these, we defined four parameters to characterise the measured absorption curves; 1) the magnitude difference, 2) the frequency difference, 3) the magnitude average and, 4) the frequency average (Figure 4.9):

$$a_m^1 = (P^\pi - P^0), \quad a_m^2 = (f_e^\pi - f_e^0), \quad (4.1)$$

$$a_m^3 = \frac{1}{2} (P^\pi + P^0), \quad a_m^4 = \frac{1}{2} (f_e^\pi + f_e^0). \quad (4.2)$$

Here,  $a_m^1$ ,  $a_m^2$ ,  $a_m^3$ , and  $a_m^4$  refer to the four parameters,  $P^\pi$ ,  $P^0$  refer to the measured magnitude (in dB) of the  $\pi$ -mode's and 0-mode's absorption line and  $f_e^\pi$ ,  $f_e^0$  refer to the  $\pi$ -mode's and 0-mode's eigenfrequency respectively (the  $\pi$ -mode is the one at near 2.998GHz).

The values  $P^\pi$ ,  $P^0$ ,  $f_e^\pi$  and  $f_e^0$  are found by fitting second order polynomials to the measured absorption lines (using the same methods as used by our PPF-script; Section 3.4.1). Using high resolution scans, we have determined them to have accuracies of about  $\pm 0.2$ dB and  $\pm 200$ Hz respectively (even though the original scans used resolutions of 25/3kHz). After having defined these parameters for our simulated absorption curves as well (with accuracies of about  $\pm 0.05$ dB and  $\pm 50$ Hz), we have minimised the differences between measurement and simulation (that is;  $a_m^i - a_s^i = \delta a^i \rightarrow 0$ , where  $i$  is the parameter number and  $a_m^i$ ,  $a_s^i$  are the parameters from the measured and simulated absorption spectra respectively).



	$f_e^\pi$ GHz	$P^\pi$ dB	$f_e^0$ GHz	$P^0$ dB	$\Delta Z_a$ mm	$\Delta R_l$ $\mu$ m	$\Delta T_f$ °C
1	2.998966	-16.5	2.992573	-11.4	-1.136	1.5	2.95
2	2.997820	-18.1	2.991435	-10.7	-0.914	2.7	1.25
3	2.998966	-16.7	2.992574	-11.4	-1.110	1.5	3.00
4	2.997822	-18.0	2.991434	-10.9	-0.949	2.7	1.33
5	2.998198	-17.6	2.991810	-11.0	-0.994	2.4	1.77
6	2.998580	-17.2	2.992188	-11.0	-1.032	2.0	2.28

Table 4.2: Overview of spectrum values and used correction factors.

For this, we have used three degrees of freedom. The first degree of freedom used is the antenna's position (the same as the one mentioned in our PPF-scan example; [Section 3.4.1](#)). This one mostly influences  $\alpha_s^1$ , and  $\alpha_s^3$ . The second one (the ratio between the cell's diameters) is used to tune  $\alpha_s^2$ , and a third one (the cavity's fabrication temperature), is used to set  $\alpha_s^4$ . These degrees of freedom are orthogonal enough to allow for three simultaneous root finding algorithms (each one optimising one degree of freedom). As stop criteria we have used  $\delta\alpha^1$ ,  $\delta\alpha^3 < 0.1$  dB and  $\delta\alpha^2$ ,  $\delta\alpha^4 < 400$  Hz. The resulting fit is shown in [Figure 4.10](#).

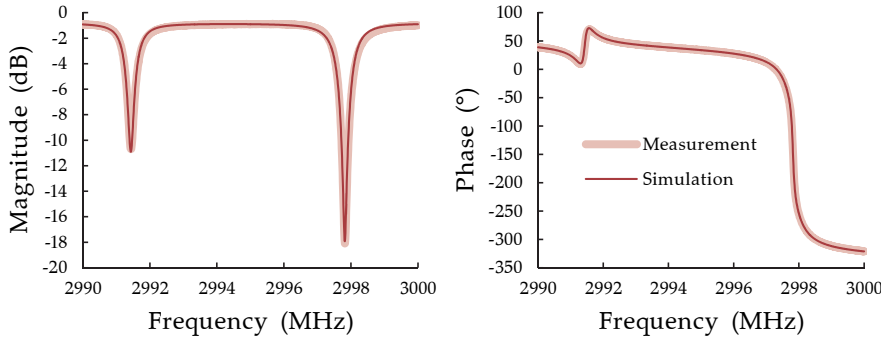


Figure 4.10: Comparison of measurement and simulation (with correction).

For each measurement (numbered the same as in [Table 4.1](#)), the resulting eigenfrequencies, absorption line magnitudes and correction factors are listed in [Table 4.2](#). Here,  $\Delta Z_a$  refers to the position of the antenna (in millimetres at 20°C), relative to the design value (3.164 mm, at 20°C). A negative value corresponds to a position closer to the iris. Furthermore,  $\Delta R_l$  and  $\Delta R_r = -\Delta R_l$  denote the radii corrections of the left and right cell respectively (positive means larger), and  $\Delta T_f$  is the correction of the fabrication temperature (a positive value means a higher fabrication temperature and thus a smaller cavity at the reference temperature; 20°C).

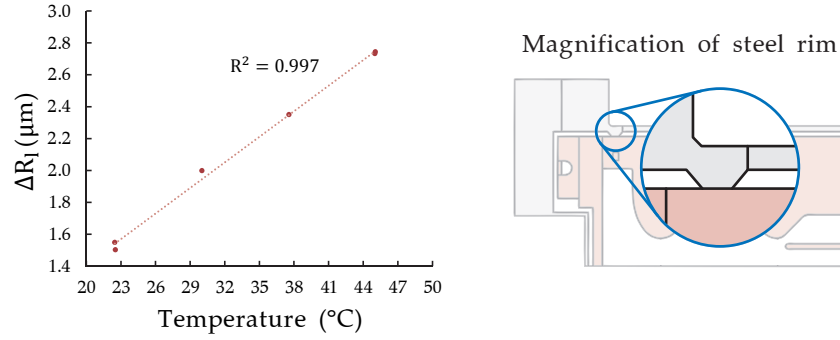


Figure 4.11: Temperature dependence of  $\Delta R_l$  and location of steel rim.

When comparing Table 4.1 and Table 4.2 it appears that the correction factors depend linearly on temperature. The temperature dependence of the antenna's correction factor  $\Delta Z_a$  is the one least significant and most easily explained:  $\Delta Z_a$  becomes smaller with increasing temperature, suggesting that in the simulations the antenna heats up and expands more than in reality. Given that we do not know the antenna's actual temperature and given that the temperature of the one in our model had to be based partly on guess work, the simulations seem adequate: They suggest the real antenna is placed  $1.0 \pm 0.1\text{ mm}$  closer to the iris than the one in the design drawings (which is not unlikely since its position has been adjusted several times).

The explanation for the temperature dependence of  $\Delta R_l$  is less obvious however. It appears that  $\Delta R_l$  increases with increasing temperature (Figure 4.11). Apparently, the left cell doesn't expand enough in the simulations. A possible explanation could be the presence of a stainless steel rim between the vacuum chamber and the cavity, limiting the expansion of the left cell (Figure 4.11, it has a lower temperature and a lower thermal expansion coefficient). Since the photogun's design drawings aren't clear about the mechanical and thermal contact between the rim and the cavity, we may reduce the rim without losing validity (creating a gap between rim and cavity). The resulting values for two of the six measurements are listed in Table 4.3.

#### 4.3.3 Discussion

Table 4.3 shows fairly constant values for  $\Delta R_l$ . Assuming the initial model represents the original design and the fitted model represents the actual setup, this suggests the left cell's radius is  $1.2\text{--}1.3\mu\text{m}$  larger than originally intended (meaning the right one is equally smaller). As a side effect, the temperature correction becomes stable as well (note that the temperature and radius corrections are interchangeable; a temperature correction of  $1^\circ\text{C}$  equals a radius correction of about  $0.7\mu\text{m}$ ). The resulting model reproduces the measured values quite well over a temperature interval of more than  $20^\circ\text{C}$ .

	$f_e^\pi$ GHz	$P^\pi$ dB	$f_e^0$ GHz	$P^0$ dB	$\Delta Z_a$ mm	$\Delta R_l$ $\mu$ m	$\Delta T_f$ °C
3	2.998966	-16.7	2.992574	-11.4	-1.110	1.3	3.22
4	2.997822	-18.0	2.991434	-10.9	-0.965	1.2	3.01

Table 4.3: Overview of results obtained using a reduced steel rim.

#### 4.4 PHASE THERMOSTRATION

When examining measurements 3 and 4, we see that the spectrum shifts with about 50kHz/°C (as it should considering the thermal expansion coefficients used). Furthermore, when looking at the phase curve depicted in [Figure 4.10](#), we see that within a small frequency interval (about 70kHz), the phase becomes linearly dependent ( $R^2 = 0.999$ ) on the frequency (with a slope of about  $-1.2^\circ/\text{kHz}$ ).

Now; if we measure the phase of the reflected signal at one specific frequency (close to the eigenfrequency), a temperature change of 1°C leads to a phase change of about  $50 \cdot 1.2 = 60^\circ$ . Therefore, monitoring the phase should be an accurate way to detect temperature changes: It could greatly improve cavity thermostration. To investigate this, we have done several measurements regarding phase stability.

##### 4.4.1 *Measuring*

Measuring the temperatures and resonance behaviour has been done the same way as for the other experiments ([Section 4.2.1](#), [Section 4.3.1](#); using our multichannel thermometer and network analyser). However, we now deliberately create temperature changes of  $\pm 0.4^\circ\text{C}$  by varying the current through the heating wire every 15-30 minutes. The resulting temperature and phase changes have been measured during extended periods of time (up to several hours).

One of the results is depicted in [Figure 4.12](#). Here, we have converted the phase signal to degrees Celsius, using the coefficient of proportionality mentioned before ( $60^\circ/^\circ\text{C}$ ). As we can see, the converted phase curve follows the same pattern as the thermocouples, but with better stability. Stationary measurements suggest the noise on the phase signal has a standard deviation of about  $0.1^\circ$ , corresponding to  $0.002^\circ\text{C}$ ; certainly more stable than the thermocouples and (to a lesser extent) the LM35 sensors. This, indeed, promises to be a very accurate way of determining temperature fluctuations.

##### 4.4.2 *Discussion*

There are some things to consider however: First, the network analyser uses fairly small bandwidths (10kHz-300Hz) and low power levels;

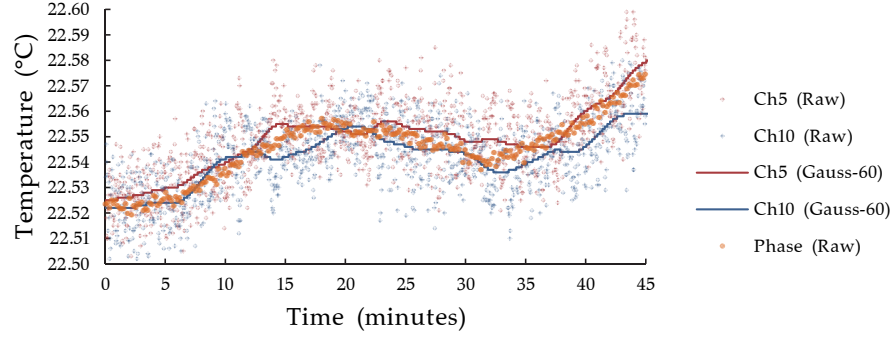


Figure 4.12: Long-term temperature reading with phase values.

we haven't tested the system in combination with high-power broadband klystron pulses.

Secondly, depending on where the phase is measured, the waveguide temperature might introduce additional errors. Suppose we have 5m waveguide between the measurement device and the cavity; the difference in optical path length between incoming and reflected signal is then 10m. If the waveguide's temperature increases by  $1^{\circ}\text{C}$ , the difference in optical path length changes with

$$\Delta L = L\alpha\Delta T \approx 1.69 \cdot 10^{-4} \text{m} \approx 1.69 \cdot 10^{-3} \lambda,$$

with  $\alpha$  the thermal expansion coefficient of copper and  $\lambda$  the wavelength at 2.998GHz; 10cm. This means that a fluctuation in the waveguide's temperature of  $1^{\circ}\text{C}$  leads to a phase fluctuation of about  $0.6^{\circ}$  (or when converted to cavity temperature;  $0.01^{\circ}\text{C}$ ).

Thirdly, phase thermostroation can only be applied in a relative sense: Although the measured phase can be used for stabilising the temperature once it has reached its correct level, finding this level will have to be done using other means. This is because the phase shows linear behaviour in an interval of about 70kHz. If one were to use the derivative of the phase curve (a bell shaped curve having a minimum at the eigenfrequency) to determine the eigenfrequency (and thus the absolute temperature), one finds this is only possible with an accuracy of about  $\pm 35\text{kHz}$ , or  $\pm 0.7^{\circ}\text{C}$  (besides, since the signal may be quite noisy, it's derivative may show large spikes).

We have further found that the success of this technique greatly depends on the coupling between coaxial line and cavity. If we change this coupling in the simulations by moving the antenna to a more optimal position (as done in [Section 3.4.1](#)), the reflected power will approach zero and the phase becomes undefined ([Figure 4.13](#)). On both sides of this point of optimum coupling, the phase curve's derivative shows asymptotically rising and descending behaviour. This is also evident from the lumped element model, discussed in [Section 2.2](#).

When combined with noise, asymptotic behaviour may lead to unstable behaviour (to prevent this, one should use sub-optimal coupling). On the plus side however, this effect allows us to tune the

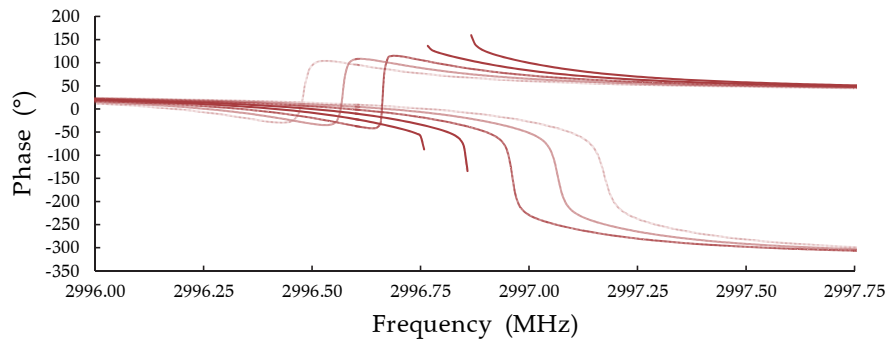


Figure 4.13: Phase curve on both sides of point of optimum coupling.

system's sensitivity (the ratio  $^{\circ}/^{\circ}\text{C}$ ) by adjusting the position of the antenna. An adjustable antenna (without dismantling) would therefore be preferable. All in all, phase thermostration appears to be a promising technique and should be investigated further, preferably using fully operational RF-photoguns.



## CONCLUSIONS AND RECOMMENDATIONS

---

As part of a design study for a compact high rep-rate soft X-ray Free Electron Laser at the University of Groningen (ZFEL)<sup>1</sup>, we have performed an initial feasibility study of high rep-rate RF-photoguns: We have developed and benchmarked numerical models (finite element) that describe the dissipation of electromagnetic energy, heat transport and thermal expansion. The models are able to reproduce existing (low rep-rate) results and allow for studies in the high rep-rate domain. Below, we list our most important conclusions and recommendations:

- Lumped element description: A lumped element description rather accurately reproduces the cavity's resonance behaviour (Section 2.2.2). It has helped us understanding the influence of the antenna's position on phase thermostratation (Section 4.4.2).
- PPF-Scan example: Our optimisation methods suggest the antenna's optimal position to be 3.425mm (at 40°C), instead of its design value (3.165mm, Section 3.4.2). The influence of the antenna's position is limited however; both simulations (the 3.165mm one as well as the 3.425mm one) agree fairly well with the design values (Table 3.1).
- Temperature gradient measurements: Several practical limitations (listed in Section 4.2.3) led us to believe that, regarding heat transport, numerical as well as experimental prototypes should be used during the development stages of high rep-rate photoguns. When developing a photogun for ZFEL, special interest should go to experimentally obtaining accurate input parameters for the used models. Only then will they be accurate enough to realistically simulate the gun's extreme conditions.
- Reflection measurements: Our electromagnetic wave simulations have shown not one single unaccountable or uncorrectable flaw (Section 3.3 and Section 4.3.3). Given that the used thermal model is proven to be solid, adding wave phenomena should not lead to any difficulties.
- Phase thermostratation: Phase thermostratation appears to be a promising technique and should be investigated further. More research is needed, preferably on fully operational RF-photoguns.

---

<sup>1</sup> <http://www.rug.nl/kvi/experimentalfacilities/zfel/index>





## NUMERICAL METHODS

---

During our studies, we have used different numerical methods (as explained in [Section 3.1](#)); the Finite Difference Method (FDM) and the Finite Element Method (FEM) [5, p. 589-600]. This appendix will give a short introduction to both.

### A.1 HEAT EQUATION

In order to illustrate the main concepts of these methods we will use a simple, one dimensional version of the heat equation. In mathematics, the heat equation is the prototypical parabolic partial differential equation. We will include a short, intuitive description here.

First, a difference in temperature (as a function of location) results in a flow of heat;

$$\vec{q}(l, t) = -k \frac{\partial u(l, t)}{\partial l}, \quad 0 < l < L,$$

where  $\vec{q}(l, t)$  represents the heat flow,  $k$  represents the thermal conductivity of the material,  $\partial u(l, t) / \partial l$  represents the heat gradient and  $L$  is chosen as the total length of the domain (we assume no work is done and there are neither heat sources nor sinks).

Then, at any given point along our domain a variation in this heat flow (again, as a function of location) will result in an accumulation or dissipation of thermal energy over time. Given a constant heat capacity of the material, this will result in an increasing or decreasing temperature;

$$\rho c_p \frac{\partial u(l, t)}{\partial t} = -\frac{\partial \vec{q}(l, t)}{\partial l}, \quad 0 < l < L, \quad \forall t > 0,$$

where  $\rho$  represents the mass density of the material and  $c_p$  represents the specific heat capacity. The combination of these two principles completes our heat equation;

$$\frac{\partial u(l, t)}{\partial t} = \frac{k}{\rho c_p} \left( \frac{\partial^2 u(l, t)}{\partial l^2} \right),$$

or, equivalently,

$$\frac{\partial u(l, t)}{\partial t} - \alpha \frac{\partial^2 u(l, t)}{\partial l^2} = 0, \quad 0 < l < L, \quad \forall t > 0, \quad (\text{A.1})$$

where the coefficient  $\alpha$  is called the thermal diffusivity of the material. [Equation A.1](#) still gives a somewhat general description. If we want

it to apply to a specific situation we will have to add some boundary conditions;

$$u(0, t) = T_0, \quad u(L, t) = T_L, \quad \forall t \geq 0, \quad (\text{A.2})$$

and an initial condition;

$$u(l, 0) = u_s(l), \quad 0 \leq l \leq L. \quad (\text{A.3})$$

Consequently, one can view our desired result  $u(l, t)$  as being a two dimensional scalar field with three of its four boundaries fixed. The fourth boundary  $u(l, t_e)$  and the surface in between will be determined by our heat equation and our stop criteria.

## A.2 STANDARD FORM

Before proceeding with an introduction to FDM and FEM, we will first convert our scalar field  $u(l, t)$  into a standard form  $w(x, t)$ , by shrinking and tilting it. For reasons that will become apparent later on, the form  $w(x, t)$  will be easier to implement in both methods.

First, we shrink our domain from  $[0, L]$  to  $[0, 1]$  by setting  $l = xL$ , substituting and changing from variable  $l$  to variable  $x$ ;

$$u(l, t) = u(xL, t) = v(x, t), \quad 0 < x < 1, \quad \forall t > 0.$$

We then proceed by choosing a straight line that interpolates the values at the end points;  $v_l(x) = xT_L + (1 - x)T_0$  and subtracting it from our desired solution;  $v(x, t) - v_l(x) = w(x, t)$ . The result is a function  $w(x, t)$ , defined on a standard interval  $[0, 1]$ , having standard boundary conditions

$$w(0, t) = w(1, t) = 0, \quad \forall t \geq 0, \quad (\text{A.4})$$

and the initial condition

$$w(x, 0) = w_s(x), \quad 0 \leq x \leq 1. \quad (\text{A.5})$$

As it turns out, in order to determine  $u(l, t)$  it is sufficient to solve

$$\frac{\partial w(x, t)}{\partial t} - \alpha \frac{\partial^2 w(x, t)}{\partial x^2} = 0, \quad 0 < x < 1, \quad \forall t > 0, \quad (\text{A.6})$$

using the conditions from [Equation A.4](#) and [Equation A.5](#).

Once the field  $w(x, t)$  is known, one can choose to convert back to the original form  $u(l, t)$ , by adding  $v_l(x)$  again and by changing back from variable  $x$  to  $l$ . The idea that adding and subtracting  $v_l(x)$  has no effect on the outcome may sound a bit counter intuitive, but bear in mind that  $v_l(x)$  has no first derivative with respect to time and no second derivative with respect to position. It will therefore vanish in [Equation A.6](#).

## A.3 FINITE DIFFERENCE METHOD

One way of solving Equation A.6 is by using the finite difference method. We start by introducing the nodes  $\{x_i\}_{i=0}^n$  given by  $x_i = ih$ , where  $n \geq 2$  is an integer and  $h = 1/n$  is the node spacing. We then proceed by replacing  $\partial^2 w(x, t) / \partial x^2$  by the second order centred finite difference;

$$\begin{aligned} \frac{\partial w_i(t)}{\partial t} - \alpha \frac{w_{i-1}(t) - 2w_i(t) + w_{i+1}(t)}{h^2} &= 0, & 0 < i < n, \\ & & \forall t > 0, \\ w_0(t) = w_n(t) &= 0, & \forall t \geq 0, \\ w_i(0) &= w_s(x_i), & 0 \leq i \leq n. \end{aligned}$$

where the functions  $w_i(t)$  approximate the exact solutions  $w(x_i, t)$ .

In effect, we have now applied space discretisation, converting our problem into a system of ordinary differential equations;

$$\begin{cases} \frac{\partial}{\partial t} \begin{bmatrix} w_1(t) \\ \vdots \\ w_{n-1}(t) \end{bmatrix} + \frac{\alpha}{h^2} \begin{bmatrix} 2 & -1 & & \\ -1 & 2 & \ddots & \\ & \ddots & \ddots & \ddots \end{bmatrix} \begin{bmatrix} w_1(t) \\ \vdots \\ w_{n-1}(t) \end{bmatrix} = 0, \\ \begin{bmatrix} w_1(0) \\ \vdots \\ w_{n-1}(0) \end{bmatrix} = \begin{bmatrix} w_s(x_1) \\ \vdots \\ w_s(x_{n-1}) \end{bmatrix}, \end{cases}$$

or, equivalently,

$$\begin{cases} \frac{\partial \vec{w}(t)}{\partial t} + \alpha A_{fd} \vec{w}(t) = 0, & \forall t > 0, \\ \vec{w}(0) = \vec{w}_s, \end{cases} \quad (\text{A.7})$$

where  $A_{fd}$  is the symmetric finite difference matrix. We then proceed by introducing a new integer  $k \geq 0$  and set  $\vec{w}^k = \vec{w}(k\Delta t)$ . This allows us to replace  $\partial \vec{w}(t) / \partial t$  by a finite difference as well and follow the forward Euler scheme;

$$\begin{cases} \frac{\vec{w}^{k+1} - \vec{w}^k}{\Delta t} + \alpha A_{fd} \vec{w}^k = 0, & \forall k \geq 0, \\ \vec{w}^0 = \vec{w}_s. \end{cases} \quad (\text{A.8})$$

Although the forward Euler scheme is not our most stable option (it is only stable iff  $\Delta t < h^2/2\alpha$ ), it does have the nice advantage of giving each following vector explicitly;  $\vec{w}^{k+1} = (I - \alpha\Delta t A_{fd}) \vec{w}^k$ . This allows us to start with  $\vec{w}^0 = \vec{w}_s$  and see how our vector  $\vec{w}^k$  develops over time by recursively multiplying it by the matrix  $(I - \alpha\Delta t A_{fd})$ . An approximate answer to Equation A.6 in the form of  $\tilde{w}(x, t)$  can then be determined by taking the points  $\{\{w_i^k\}_{i=0}^n\}_{k=0}^{t_e/\Delta t}$  and interpolating where necessary (using polynomials).

## A.4 FINITE ELEMENT METHOD

The finite element method is generally a more powerful tool than the finite difference method. It is a better choice for solving partial differential equations in cases having complex geometries, deforming geometries or varying desired precision. Since illustrating the true power of this method lies beyond the scope of this text, we will restrict ourselves to a simplified description of the method's concepts.

First, we will denote by  $V$  a test function space. This space consists of all functions  $v(x)$  that are continuous on  $[0, 1]$ , vanish at  $x = 0$  and  $x = 1$  and whose first derivative is piecewise continuous, i.e., continuous everywhere except at a finite number of points in  $[0, 1]$  where the left and right limits  $(\partial v(x)/\partial x)_-$  and  $(\partial v(x)/\partial x)_+$  exist but do not necessarily coincide. Using nontrivial proofs, one can determine  $V$  to be a Hilbert space, which is denoted by  $H_0^1(0, 1)$ . More precisely,

$$H_0^1(0, 1) = \{v(x) \in L^2(0, 1) : \partial v(x)/\partial x \in L^2(0, 1) : v(0) = v(1) = 0\},$$

where  $L^2$  indicates the space of square-integrable functions (note that  $\partial v(x)/\partial x$  can only be part of  $L^2$  in a piecewise sense).

The functions inside this Hilbert space are considered to be infinitely dimensional vectors where every value of  $x$  represents one dimension. Consequently, an inner product can be defined as

$$[f(x_0) \cdots f(x_\infty)] \begin{bmatrix} g(x_0) \\ \vdots \\ g(x_\infty) \end{bmatrix} = \langle f, g \rangle = \int_0^1 f \bar{g} dx.$$

After having determined our function space and its inner product, we will proceed by multiplying [Equation A.6](#) by one of the test functions  $v = v(x)$  and integrate over  $[0, 1]$ ;

$$\int_0^1 \frac{\partial w(x, t)}{\partial t} v(x) dx - \alpha \int_0^1 \frac{\partial^2 w(x, t)}{\partial x^2} v(x) dx = 0, \quad \begin{array}{l} \forall t > 0, \\ w \in V, \\ \forall v \in V. \end{array}$$

Then, by using integration by parts we obtain

$$\int_0^1 \frac{\partial w(x, t)}{\partial t} v(x) dx + \alpha \int_0^1 \left( \frac{\partial w(x, t)}{\partial x} \right) \left( \frac{\partial v(x)}{\partial x} \right) dx = 0, \quad (\text{A.9})$$

for all  $t > 0$ , where we have used the assumption that  $v(0) = v(1) = 0$ . This result is called the weak formulation of our problem [Equation A.6](#). Since it contains only the first derivative of  $w(x, t)$ , it might cover cases in which a classical solution to our problem does not exist although the physical problem itself is well defined.

Space discretisation (discretisation of the  $x$  variable) will take place by moving to a finite dimensional subspace of  $V$  called  $V_h$ . In order

to do this, we take the interval  $[0, 1]$ , choose  $n - 1$  values for  $x$  (not necessarily equidistant) with  $0 = x_0 < x_1 < \dots < x_n = 1$  and set the subintervals  $I_i = [x_i, x_{i+1}]$ . We now can define our piecewise polynomial space to be

$$V_h = \{v_h(x) : [0, 1] \rightarrow \mathbb{R} : v_h(x)|_{I_i} \in \mathbb{P}_1(I_i), \quad 0 \leq i < n \\ : v_h(0) = v_h(1) = 0\},$$

with  $\mathbb{P}_1$  the space of first order polynomials. In other words, each function within collection  $V_h$  consists of linear segments that connect the dots  $\{v_h(x_i)\}_{i=0}^n$  (note that, in order to create smoother results, we could also have chosen  $\mathbb{P}_2$  or higher order polynomials).

To complete the discretisation, we must select a basis of  $V_h$ . For each node  $x_i$ ,  $0 < i < n$ , we choose a piecewise linear function  $\varphi_i(x) \in V_h$  whose value is 1 at  $x_i$  and 0 at  $x_j$ ,  $j \neq i$ , i.e.,

$$\varphi_i(x) = \begin{cases} \frac{x - x_{i-1}}{x_i - x_{i-1}} & \text{for } x_{i-1} \leq x \leq x_i, \\ \frac{x_{i+1} - x}{x_{i+1} - x_i} & \text{for } x_i \leq x \leq x_{i+1}, \\ 0 & \text{elsewhere,} \end{cases}$$

for  $0 < i < n$ . This results in  $n - 1$  tent functions  $\{\varphi_i(x)\}_{i=1}^{n-1}$ , who's linear combination may describe any function from the collection  $V_h$ , including our approximate answer;

$$w_h(x, t) = \sum_{j=1}^{N_h} w_j(t) \varphi_j(x),$$

with  $w_j(t) = w_h(x_j, t)$ ,  $0 < j < n$ , the unknown coefficients and  $N_h = n - 1$  the dimension of the finite element space  $V_h$ .

We can then approximate [Equation A.9](#) by

$$\int_0^1 \frac{\partial w_h(x, t)}{\partial t} v_h(x) dx + \alpha \int_0^1 \left( \frac{\partial w_h(x, t)}{\partial x} \right) \left( \frac{\partial v_h(x)}{\partial x} \right) dx = 0, \\ \int_0^1 \sum_{j=1}^{N_h} \frac{\partial w_j(t)}{\partial t} \varphi_j(x) \varphi_i(x) dx \\ + \alpha \int_0^1 \sum_{j=1}^{N_h} w_j(t) \left( \frac{\partial \varphi_j(x)}{\partial x} \right) \left( \frac{\partial \varphi_i(x)}{\partial x} \right) dx = 0, \quad 0 < i \leq N_h,$$

for all  $t > 0$ , where we have chosen  $v_h(x)$  to be the whole basis  $\{\varphi_i(x)\}_{i=1}^{n-1}$ .

Once again, we can convert our result to a system of ordinary differential equations;

$$\begin{aligned} & \sum_{j=1}^{N_h} \frac{\partial w_j(t)}{\partial t} \int_0^1 \varphi_j(x) \varphi_i(x) dx \\ & + \alpha \sum_{j=1}^{N_h} w_j(t) \int_0^1 \left( \frac{\partial \varphi_j(x)}{\partial x} \right) \left( \frac{\partial \varphi_i(x)}{\partial x} \right) dx = 0, \\ & \sum_{j=1}^{N_h} \frac{\partial w_j(t)}{\partial t} m_{ij} + \alpha \sum_{j=1}^{N_h} w_j(t) a_{ij} = 0, \quad 0 < i \leq N_h, \quad \forall t > 0, \end{aligned}$$

or, equivalently,

$$\begin{cases} M \frac{\partial \vec{w}(t)}{\partial t} + \alpha A_{fe} \vec{w}(t) = 0, & \forall t > 0, \\ \vec{w}(0) = \vec{w}_s, \end{cases} \quad (\text{A.10})$$

where  $M = m_{ij} = \int_0^1 \varphi_j(x) \varphi_i(x) dx$  and  $A_{fe} = a_{ij} = \int_0^1 (\partial \varphi_j(x) / \partial x) (\partial \varphi_i(x) / \partial x) dx$  for  $j, i = 1, \dots, N_h$  are the matrixes containing the inner products of the space  $V_h$ . The matrix  $M$  is also known as the mass matrix, whereas the matrix  $A_{fe}$  is known as the stiffness matrix.

Time discretisation can now be done by proceeding in exactly the same manner as was done for [Equation A.7](#) (note the similarities between [Equation A.7](#) and [Equation A.10](#)). After following the forward Euler scheme, one can once again determine an approximate answer to [Equation A.6](#) in the form of  $\tilde{w}(x, t)$  by taking the determined points  $\{\{w_i^k\}_{i=0}^n\}_{k=0}^{t_e/\Delta t}$  and interpolate where necessary using polynomials.

## EXAMPLES

### B.1 3D RF-PSCAN (COUPLER, RECTPORT)

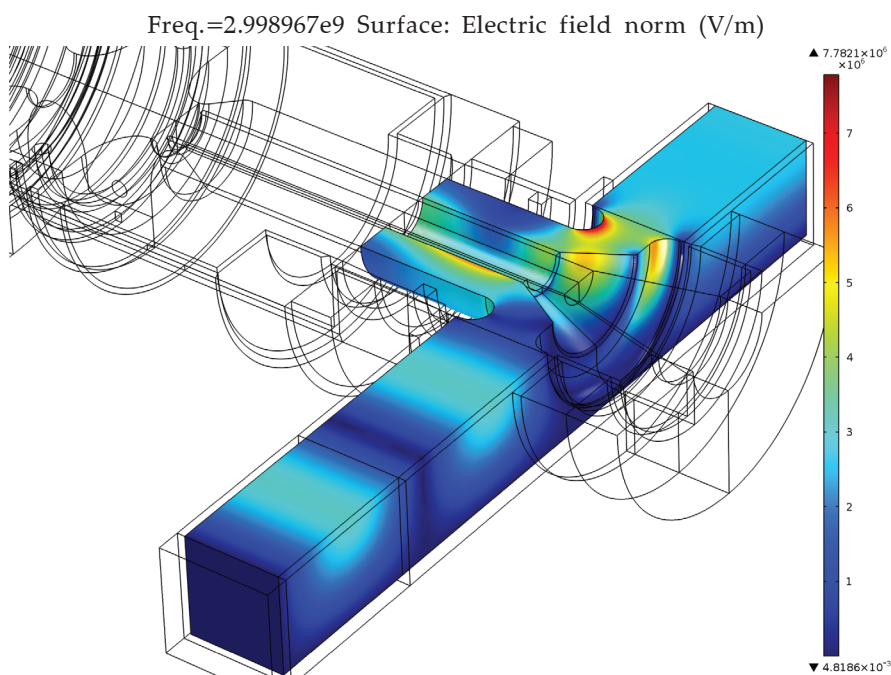


Figure B.1: Electric field plot of the input coupler (3D).

- Electromagnetic wave simulation (no heat and expansion).
- Average mesh size: 3.9mm (min: 0.4mm, max: 11.4mm).
- Time needed: 3 minutes, 16 seconds.
- Memory needed: 7.62GB (RAM memory installed: 16GB).
- Temperature: 293.15K.
- Frequency: 2.998966511GHz.
- Rectangular power in: 8.296MW.
- Absorbed by rectangular waveguide and doorknob: 13.156kW.
- Coaxial power out: 8.279MW (throughput efficiency: 99.8%).
- Wall electric field peak: 7.789MV/m.
- Optimal stop position relative to doorknob centre: 166.7mm.

## B.2 2D RF-SIM (CAVITY, COAXPORT)

Freq.=2.998957e9 Surface: Electric field norm (V/m)

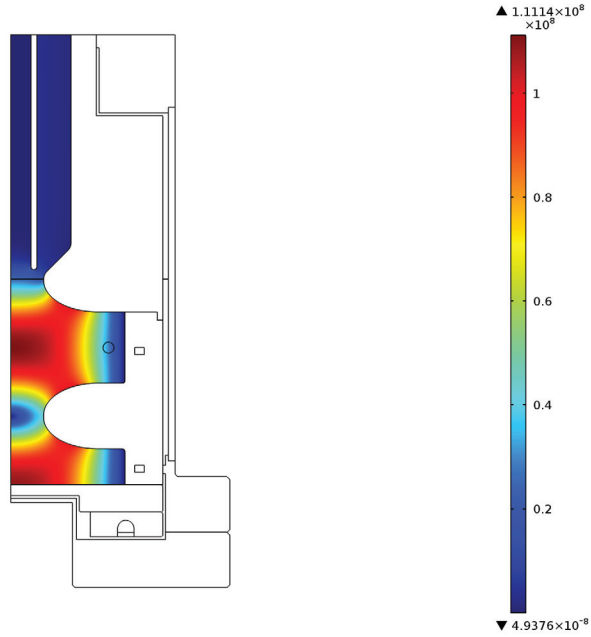


Figure B.2: Electric field plot of the cavity (2D).

- Electromagnetic wave simulation (no heat and expansion).
- Average mesh size: 0.6mm (min: 0.2mm, max: 0.8mm).
- Time needed: 7 seconds.
- Memory needed: 1030MB (RAM memory installed: 16GB).
- Temperature: 293.15K.
- Frequency: 2.998957330GHz (1.032830MHz rel. to 10c).
- Coaxial power in: 8.306MW.
- Absorbed by coaxial line: 5.261kW.
- Entering the cavity: 8.298MW.
- Absorbed in the cavity: 8.301MW.
- Energy in the cavity: 5.105J.
- 0.5 Cell electric field peak: 108.851MV/m.
- 1.0 Cell electric field peak: 111.149MV/m.
- Wall electric field peak: 100.997MV/m.
- Total voltage gain: 5.721MV.
- Unloaded quality factor: 11588.551.
- Shunt impedance: 50.355M $\Omega$ /m.
- R over Q: 4.345k $\Omega$ /m.
- Optimal antenna position relative to iris: 3.47mm.



## B.3 3D RF-SIM (CAV+COUP, RECTPORT)

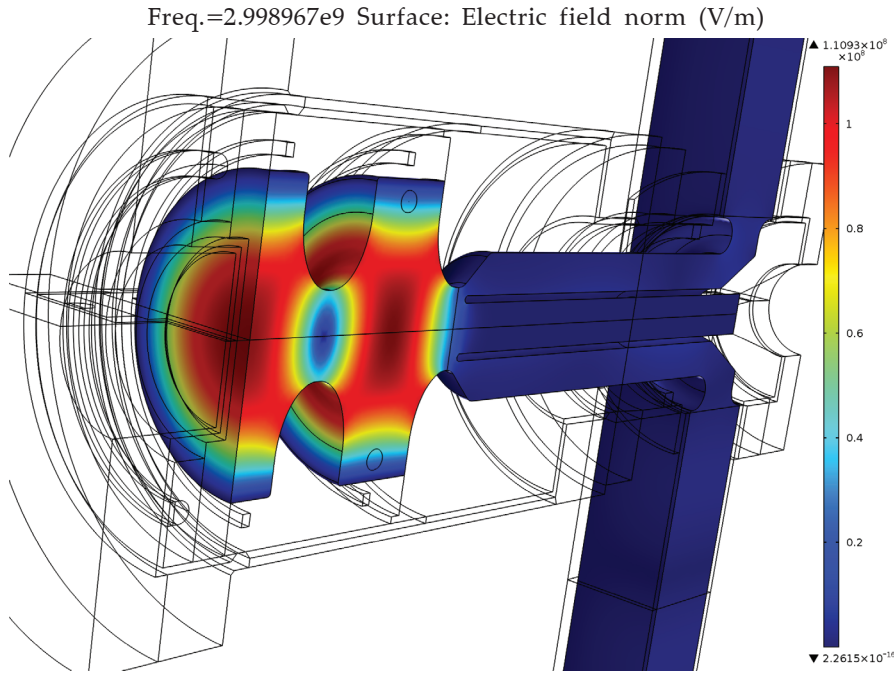


Figure B.3: Electric field plot of cavity and coupler (3D).

- Electromagnetic wave simulation (no heat and expansion).
- Average mesh size: 3.9mm (min: 0.4mm, max: 11.4mm).
- Time needed: 7 minutes, 42 seconds.
- Memory needed: 15.80GB (RAM memory installed: 16GB).
- Temperature: 293.15K.
- Frequency: 2.998966511GHz ( $9.181\text{kHz} > 2\text{D}$ ).
- Rectangular power in: 8.287MW.
- Absorbed by rectangular waveguide and doorknob: 14.106kW.
- Coaxial power in: 8.269MW ( $37.114\text{kW} < 2\text{D}$ ).
- Absorbed by coaxial line: 5.510kW ( $248.527\text{W} > 2\text{D}$ ).
- Entering the cavity: 8.252MW ( $46.451\text{kW} < 2\text{D}$ ).
- Absorbed in the cavity: 8.260MW ( $41.144\text{kW} < 2\text{D}$ ).
- Energy in the cavity: 5.079J ( $25.891\text{mJ} < 2\text{D}$ ).
- 0.5 Cell electric field peak: 108.689MV/m ( $161.855\text{kV/m} < 2\text{D}$ ).
- 1.0 Cell electric field peak: 111.003MV/m ( $145.792\text{kV/m} < 2\text{D}$ ).
- Wall electric field peak: 101.745MV/m ( $747.654\text{kV/m} > 2\text{D}$ ).
- Total voltage gain: 5.706MV ( $14.591\text{kV/m} < 2\text{D}$ ).
- Unloaded quality factor: 11587.224 ( $1.327 < 2\text{D}$ ).
- Shunt impedance: 50.349M $\Omega$ /m ( $7.283\text{k}\Omega/\text{m} < 2\text{D}$ ).
- R over Q: 4.345k $\Omega$ /m (same as 2D).

## B.4 2D HEAT-SIM (CAVITY, COAXPORT)

Surface: Temperature (°C)

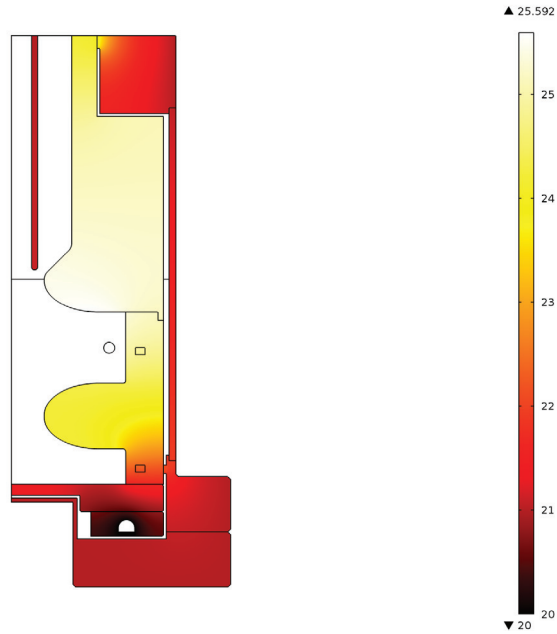


Figure B.4: Thermal plot of the cavity (2D).

- Electromagnetic wave simulation, heat generation (no expansion).
- Average mesh size: 0.6mm (min: 0.2mm, max: 0.8mm).
- Time needed: 11 seconds.
- Memory needed: 1066MB (RAM memory installed: 16GB).
- Ambient temperature: 293.15K.
- Cooling water temperature: 293.15K.
- Outer surface boundary condition: 294.15K.
- Frequency: 2.998957330GHz (1.032830MHz rel. to 10c).
- Pulse height: 8.306MW.
- Pulse length: 3 $\mu$ s.
- Repetition rate: 10Hz.
- Coaxial power in: 249.192W (Time average).
- Heat generated in the cavity: 249.026W (Time average).
- Heat dissipated to sinks: 245.149W.
- Energy in the cavity: 153 $\mu$ J (Time average).
- 0.5 Cell thermocouple: 22.244°C (At equilibrium).
- 1.0 Cell thermocouple: 24.877°C (At equilibrium).
- Total voltage gain: 31.336kV (Time average).

## B.5 3D HEAT-SIM (CAV+COUP, RECTPORT)

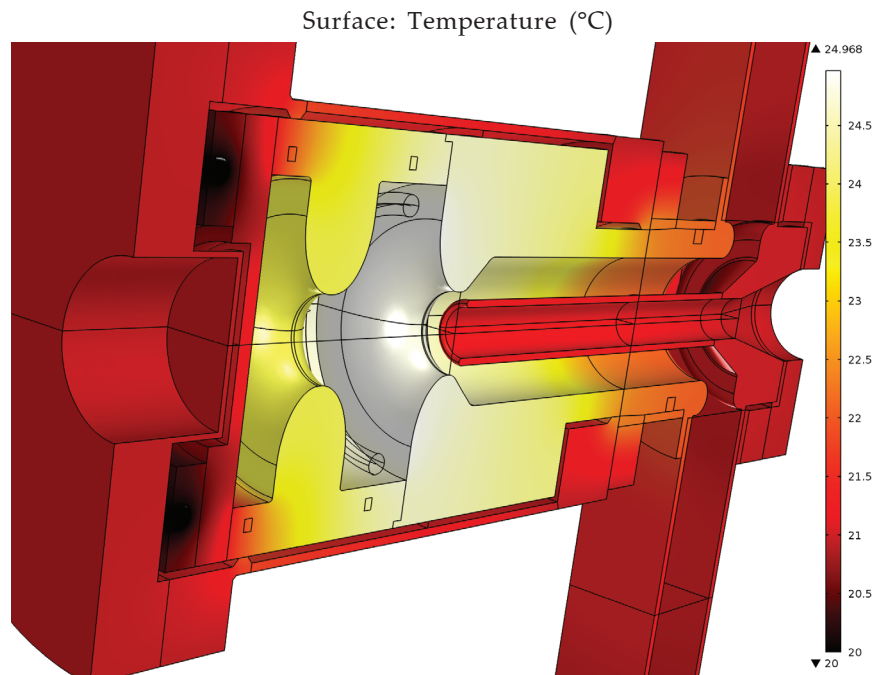


Figure B.5: Thermal plot of the cavity (3D).

- Electromagnetic wave simulation, heat generation (no expansion).
- Average mesh size: 3.9mm (min: 0.4mm, max: 11.4mm).
- Time needed: 16 minutes, 15 seconds.
- Memory needed: > 16GB (RAM memory installed: 16GB).
- Ambient temperature: 293.15K.
- Cooling water temperature: 293.15K.
- Outer surface boundary condition: 294.15K.
- Frequency: 2.998966511GHz (9.181kHz > 2D).
- Pulse height: 8.302MW (Time average, 6kW < 2D).
- Pulse length: 3μs.
- Repetition rate: 10Hz.
- Coaxial power in: 248.078W (Time average, 1.113W < 2D).
- Heat generated in the cavity: 247.792W (1.234W < 2D).
- Heat dissipated to sinks: 238.659W.
- Energy in the cavity: 152μJ (Time average, 1μJ < 2D).
- 0.5 Cell thermocouple: 22.095°C (At equilibrium, 0.149°C < 2D).
- 1.0 Cell thermocouple: 24.435°C (At equilibrium, 0.442°C < 2D).
- Total voltage gain: 31.256kV (Time average, 79.918V < 2D).



## MULTICHANNEL THERMOMETER

As explained in [Section 4.1.3](#), our experimental studies required a multichannel thermometer. This appendix will start with a description of the device itself. We then proceed with a treatment of the device during operation and conclude with some calibration procedures.

### C.1 DEVICE



Figure C.1: The LM35 sensor attached to a shielded two-wire cable.

The sensors we have used are of the semiconductor type; LM35-DZ. Their specifications are as follows:

- Calibrated directly in degrees Celsius.
- Linear  $+10.0 \pm 0.2 \text{ mV}/^\circ\text{C}$  scale factor.
- $\pm 1.5^\circ\text{C}$  accuracy guaranteed (at  $+25^\circ\text{C}$ ).
- Rated for full  $-55^\circ\text{C}$  to  $+150^\circ\text{C}$  range.
- Suitable for remote applications.
- Low cost due to wafer-level trimming.
- Operates from 4 to 30 Volts.
- Less than  $60 \mu\text{A}$  current drain.
- Low self-heating,  $0.08^\circ\text{C}$  in still air.
- Nonlinearity only  $\pm 0.25^\circ\text{C}$  typical.
- Low impedance output,  $0.1 \text{ W}$  for  $1 \text{ mA}$  load.

The LM35 sensors have three connection pins ([Figure C.1](#)): A ground connection (GND), a positive input voltage ( $+V_s$ ), and a linearly temperature dependent output voltage ( $V_{\text{out}}$ ). These have been connected (using about 60cm of shielded two-wire cable) to a printed circuit board accommodating a 16-Ch analogue multiplexer of type 4067N. In order to stabilise the readings (to drain residual voltage from the channels), a  $10 \text{ k}\Omega$  draining resistor has been added to the output. A photo of the completed device is shown in [Figure C.2](#).

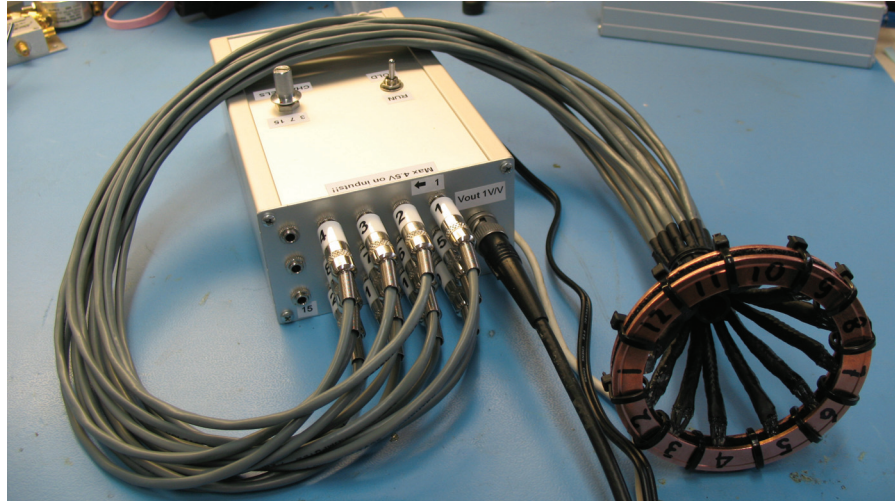
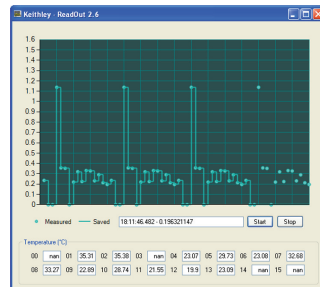


Figure C.2: The multichannel thermometer with calibration rings attached.

## C.2 OPERATION

During operation, the  $+10.0\text{mV}/^{\circ}\text{C}$  output signal from the multiplexer is fed directly into a Keithley 2000 high performance digital multimeter, that converts it to a digital reading. The Keithley is set to take a reading every 150ms, and then trigger the multiplexer to go to the next channel. The digital readouts are fed into a computer that functions as a demultiplexer; a Visual Basic script we've written analyses the continuous stream of readings (Figure C.3).



### Keithley - ReadOut 2.6:

- Connected to Keithley 2000.
- One measurement each 150ms.
- Build-in demultiplexer.
- Direct visual feedback.

Figure C.3: Graphical user interface of the demultiplexing software.

Since channel 0 is connected to a very specific, constant reference voltage (outside the scope of the LM35 sensors), it can be recognized as such (and therefore, the other 15 channels as well). When a complete dataset is detected (15 normal readings between two reference voltage readings), the Visual Basic script shows this on the screen and stores the corresponding values. When a dataset is incomplete (skipped channels), the channels cannot be identified and the dataset is discarded. This happens about once every 500 readings.



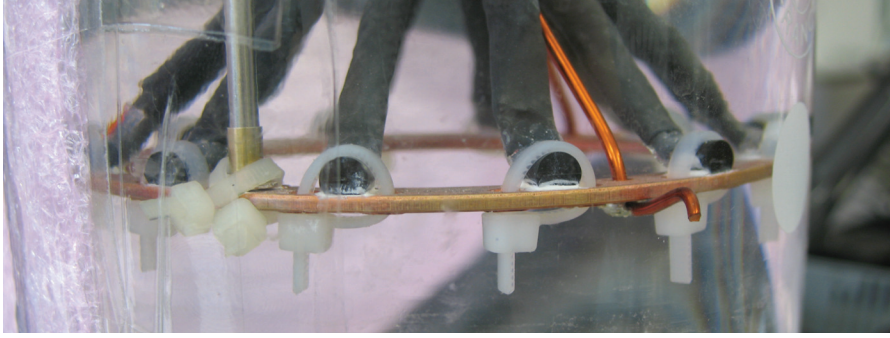


Figure C.4: Calibration setup with part of the insulation removed.

### C.3 CALIBRATION

Although the sensors have already been calibrated at the wafer level (during production), the acquired accuracy is rather poor ( $\pm 1.5^\circ\text{C}$  at  $+25^\circ\text{C}$  and  $\pm 0.2\text{mV}/^\circ\text{C}$ ). On the plus side, semiconductor temperature sensors rely on the temperature dependency of band gaps (which is linear by definition). As a consequence, we may assume the relation between the temperature and the sensor reading in millivolts equals  $T = a \cdot V_{\text{out}} + b$ , where  $T$  is the temperature in degrees Celsius,  $V_{\text{out}}$  is the LM35 output voltage in Volts,  $a \approx 100$  and  $b \approx 0^\circ\text{C}$ . What remains, is finding more accurate values for  $a$  and  $b$  (for each sensor).

Once these values have been obtained, the readings from the multimeter can be converted into the correct degrees Celsius values. This has been done entirely during post processing: During our experimental studies, all readings have been saved in Volts (the original values from the multimeter). No attempts have been made to convert the signal while measuring (except for display in the graphical user interface, [Figure C.3](#)) and no attempts whatsoever have been made to adjust the hardware itself (in such a way that  $a$  and  $b$  would show a better similarity to their respective design values). This approach has one major advantage: By applying the conversion (mV to  $^\circ\text{C}$ ) during post processing, we can (re)calibrate our system at any time using any set of measurements, without having to discard any data.

Finding  $a$  and  $b$  has been done primarily using temperature-drop and -raise measurements: The LM35 sensors have been clamped to a copper ring (ensuring a good mutual thermal contact), and placed inside an insulated reservoir of well stirred water, together with an accurate reference probe (the Testo 110, [Figure C.4](#)). During a prolonged period of time, the water is heated up and cooled down while the readings from the LM35 sensors are saved, together with a pulse signal that indicates when the last digit from the Testo reaches 0 or 5 (indicating values  $T_{\text{testo}} = \text{even}/2$  and  $T_{\text{testo}} = \text{uneven}/2$ ).

The data is then subjected (together with the Testo's starting temperatures) to linear regression analysis and the desired values  $a$  and  $b$  are extracted. To ensure better accuracy, the outcome from several

	Ch1	Ch2	Ch3	Ch4	Ch5	Ch6	Ch7
a	100.71	100.59	—	100.23	100.17	100.84	100.74
b	−0.6293	−0.0692	—	1.0821	−2.2689	0.4253	−0.6883

Table C.1: Values a and b determined for channels 1-7.

	Ch8	Ch9	Ch10	Ch11	Ch12	Ch13	Ch14
a	101.24	100.86	100.72	99.92	101.28	100.69	—
b	0.1630	−0.4540	−0.4935	0.3028	0.0246	−0.6466	—

Table C.2: Values a and b determined for channels 8-14.

temperature-drop and -raise measurements are compared and averaged. The resulting values are listed in [Table C.1](#) and [Table C.2](#).

#### C.4 DISCUSSION

Since the device has been calibrated as a whole (probes, cables, multiplexer, multimeter) the relation between sensor and channel should remain constant (swapping two sensors would effectively create a new piece of hardware and require a new calibration procedure). Furthermore, the resulting temperature values come with four different error estimates:

- An absolute error on all measurements;  $0.2^{\circ}\text{C}$ .
- A relative error between LM35 sensors ( $\Delta T < 1^{\circ}\text{C}$ );  $0.01^{\circ}\text{C}$ .
- The same for  $\Delta T > 1^{\circ}\text{C}$ ;  $0.05^{\circ}\text{C}$ .
- Contact error between probe and surface;  $0.2^{\circ}\text{C}$ .

The first one is primarily caused by an error on the reading of the reference probe itself (the Testo 110). The second one is caused by the inaccuracies of our calibration method (assuming calibration at the same time, under the same conditions), the third one is caused by inaccuracies becoming significant on larger temperature and time scales (a-linearity, changing conditions, etc.), and the fourth one is introduced in our heat gradient measurement discussion ([Section 4.2.3](#)).

Furthermore, we have discovered several LM35 sensors show a significant form of a-linear behaviour near the zero point (below  $2^{\circ}\text{C}$ ): Since they are fed by positive input voltages only, they are unable to return negative output voltages;  $V_{\text{out}}$ . As a consequence, they will return  $V_{\text{out}} \geq 0\text{V}$ , even though their linear temperature to millivolt curve might dictate otherwise.

To conclude, we should mention that the thermocouples inside the cavity walls had to be calibrated as well (one of them had an error



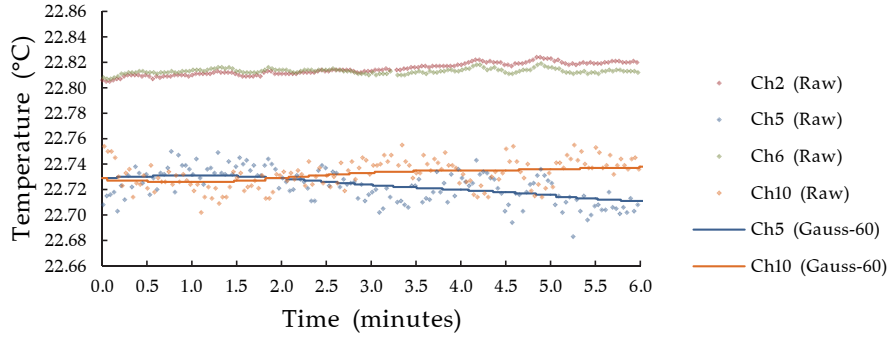


Figure C.5: Long term test reading without thermostrotration.

of over  $2^{\circ}\text{C}$ ). We have done so during post processing, using data from our reflection measurements ([Section 4.3](#)). During these measurements, the coolant and coaxial line temperatures became equal during prolonged periods of time. When combined with the assumption that (given a stationary situation) the temperature near the thermocouples should lie between these two temperatures, they gave us the correct thermocouple readings.

Since the thermocouple's signal to noise ratio is larger than the one from our LM35 sensors, their relative error estimate had to be set to  $0.05\text{-}0.10^{\circ}\text{C}$ .

As a final test, we have installed all probes, waited several days (allowing the system to reach thermal equilibrium without thermostrotration), and took several readings. One of them is depicted in [Figure C.5](#) (note that only the most relevant channels are included).



## BIBLIOGRAPHY

---

- [1] Jang-Hui Han, Matthew Cox, Houcheng Huang, and Shivaji Pande. Design of a high repetition rate s-band photocathode gun. *Elsevier*, May 2011.
- [2] John David Jackson. *Classical Electrodynamics*. John Wiley & Sons, 2nd edition, 1974.
- [3] Fred Kiewiet. *Generation of Ultra-short, High-brightness Relativistic Electron Bunches*. PhD thesis, Eindhoven University of Technology, December 2003.
- [4] Willem op 't Root. *Generation of high-field, single-cycle terahertz pulses using relativistic electron bunches*. PhD thesis, Eindhoven University of Technology, November 2009.
- [5] Alfio Quarteroni, Riccardo Sacco, and Fausto Saleri. *Numerical Mathematics*. Springer, 2nd edition, 2006.